

## **Supporting information for**

# **Developing low-resistance ion migration pathways using perfluorinated chain-decorated COFs for enhanced performance in zinc batteries**

Kun Zhang<sup>1,8</sup>, Yijia Yuan<sup>1,8</sup>, Gang Wang<sup>2,8</sup>, Fangzheng Chen<sup>1</sup>, Li Ma<sup>3</sup>, Chao Wu<sup>4</sup>, Jia Liu<sup>1</sup>, Bao Zhang<sup>5</sup>, Chenglin Li<sup>1</sup>, Hongtian Liu<sup>1</sup>, Changan Lu<sup>1</sup>, Xing Li<sup>6</sup>, Shibo Xi<sup>4</sup>, Keyu Xie<sup>3,\*</sup>, Junhao Lin<sup>2,7\*</sup>, Kian Ping Loh<sup>1,\*</sup>

<sup>1</sup>Department of Chemistry, National University of Singapore, Singapore, Singapore.

<sup>2</sup>Department of Physics and Shenzhen Key Laboratory of Advanced Quantum Functional Materials and Devices, Southern University of Science and Technology, Shenzhen, China.

<sup>3</sup>State Key Laboratory of Solidification Processing, Center for Nano Energy Materials, Northwestern Polytechnical University and Shaanxi Joint Laboratory of Graphene (NPU), Xi'an, China.

<sup>4</sup>Institute of Chemical and Engineering Sciences, Agency of Science Technology and Research, 1 Pesek Road, Jurong Island, Singapore, Singapore.

<sup>5</sup>School of Materials and Energy, University of Electronic Science and Technology of China, Chengdu, Sichuan, China.

<sup>6</sup>Department of Chemistry, City University of Hong Kong, Kowloon, Hong Kong SAR 999077, China.

<sup>7</sup>Quantum Science Center of Guangdong-Hong Kong-Macao Greater Bay Area (Guangdong), Shenzhen 518045, People's Republic of China.

<sup>8</sup>These authors contributed equally: Zhang Kun, Yuan Yijia and Wang Gang.

e-mail: [chmlohkp@nus.edu.sg](mailto:chmlohkp@nus.edu.sg); [linjh@sustech.edu.cn](mailto:linjh@sustech.edu.cn); [kyxie@nwpu.edu.cn](mailto:kyxie@nwpu.edu.cn)

## **Experimental Sections:**

**Preparation of SPCOF and SHCOF** can refer to Figure S1-S2.

**Modification of metal anode:** In this study, the modification of Li/Na/Zn anodes was carried out using a COF. Initially, the COF was mixed with PVDF at a weight ratio of 9:1 in NMP to create a uniform slurry. This slurry was then applied to the metal surface using a doctor blade coating technique. After drying and roller pressing, the COF-modified anode was punched into various sizes and utilized as the anode in the experiments described in this paper.

### **Preparation of $Zn_xV_2O_5 \cdot nH_2O$ composite and cathode**

In a typical process, A total of 15 mmol (2.728 g) of commercial  $V_2O_5$  and 12 mmol (2.140 g) of  $Zn(Ac)_2$  were dissolved in 350 mL deionized water, then 25mL acetone and 10 mL 10 wt%  $HNO_3$  were then added to the solution with wet ultrasonication in water for 5 min and vigorous stirring. The mixture was transferred to a 500 mL Teflon-lined autoclave and heated at 180°C for 36 h. After natural cooling, the obtained green powder was filtrated and washed by deionized water and ethanol for 5 times, followed by drying at 80°C for 12 h.

As prepared ZVO composites were ball milled for 3 h before fabrication cathode. Low loading ZVO cathode (loading  $\sim 1 \text{ mg cm}^{-2}$ ) is prepared by dip-casting a mixture that contained ZVO powder (70 wt%), super P carbon (20 wt%), and PVDF (10 wt%), onto Ti foil. For high loading ZVO cathode (loading  $\sim 10$  or  $20 \text{ mg cm}^{-2}$ ), the ZVO (65 wt%) was firstly coated on Ti mesh with Super P (25 wt%) and PVDF binders (10 wt%), then it was compressed by rolling machine after drying to ensure better contact. The electrodes are dried at 80 °C under vacuum for 12 h and then punched into desired size (discs of 12 mm in diameter for coin cell and  $3 \times 4 \text{ cm}^2$ ,  $7 \times 8 \text{ cm}^2$  for pouch cell).

### **Preparation of cathode for Li/Na batteries.**

For sulfur cathode, CNT/S composites (80wt% S percentage) or commercial NVP, super P conductive carbon and PVDF was mixed in NMP at a weight ratio of 8:1:1 create a uniform slurry. Then it was coated by doctor blade on Al foil to form electrode. The loading of sulfur in cathode is  $\sim 0.8 \text{ mg cm}^{-2}$  and the loading of NVP in cathode is  $\sim 2 \text{ mg cm}^{-2}$ . For Li- $CO_2$  battery, the cathode was prepared by a dip-coating

method with CNT-Ru as active materials. The typical loading is  $\sim 0.3 \text{ mg cm}^{-2}$ .

### **Assembly of coin cells and pouch cells**

Zn foils were polished with 1000 mesh sandpaper before using and modification. The thickness of Zn foil is  $50 \mu\text{m}$  (common test) and  $20 \mu\text{m}$  based on different N/P ratio and test conditions. For the Zn||ZVO coin cells at low N/P ratio (2 and 4), the all the cell is activated at a current density of  $0.1 \text{ A g}^{-1}$  during the initial 3 cycles. Then the coin cell is cycling at a rate of  $0.5 \text{ A g}^{-1}$ . The electrolyte used in this work is  $2 \text{ M ZnSO}_4$  solution (pH  $\sim 5$ ). The diameter of Zn anode is  $12 \text{ mm}$  in Zn||Zn, Zn||Cu and Zn||ZVO batteries. For coin cell, all the electrochemical properties are tested by assembling 2032-coin cells with glass fiber (GF/A) separators. For pouch cell, Ti foil ( $20 \mu\text{m}$  in thickness) is used as current collector for both anode and cathode. The amount of electrolyte added in coin cell and pouch cell were  $100 \mu\text{L}$  and  $3 \text{ mL}$  respectively.

### **Electrochemical measurements**

Galvanostatic charge and discharge measurements were carried out with Neware or Landt battery test system at different current collectors. The specific currents and discharge capacities in full cells are calculated based on the mass of active ZVO in the cathode. EIS, CV, IT and LSV was performed on an Autolab Analyzer PGSTAT 128 N (Metrohm, Switzerland). The EIS tests were measured in the potentiostatic method, the frequency is in the range from  $0.1 \text{ Hz}$  to  $100 \text{ kHz}$  at open circuit potential and an amplitude of  $5 \text{ mV}$ .

### **Structural and chemical characterizations**

X-ray diffraction data is measured by a Bruker D8 Advance with Cu-K $\alpha$  Xray radiation ( $\lambda = 0.154056 \text{ nm}$ ), using an operating voltage of  $40 \text{ kV}$  and a  $40 \text{ mA}$  current. Field-emission scanning electron microscopy (FESEM) images are acquired from a JEOL JSM-6701F. XPS measurements are carried out with a Thermo Scientific K-Alpha<sup>+</sup> spectrometer under vacuum. Raman patterns was collected in a Renishaw in via with  $532 \text{ nm}$  laser. All FT-IR spectra were recorded on a Bruker vertex 80v spectrometer. Elemental analysis was performed on Elementar vario MICRO cube for C, H, N and S. Gas sorption analysis were performed on Quantachrome Instruments Autosorb-iQ

(Boynton Beach, Florida USA) with extra-high pure gases. The samples were activated and outgassed at 120 °C for 8 h before measurement. The BET surface area and total pore volume were calculated from the N<sub>2</sub> sorption isotherms at 77 K, and the pore size distribution was calculated based on the N<sub>2</sub> sorption isotherm by using Non-Local Density Functional Theormodel in the Quantachrome ASiQwin 5.0 software package. NMR spectra were collected on a Bruker AMX400 (400 MHz) spectrometer. Chemical shifts were reported in parts per million (ppm). Residual solvent peak was used as an internal reference. Solid-state NMR experiments were performed on a 9 T Bruker Advance Neo 400 MHz wide-bore spectrometer with an Agilent 5.0 mm T3 probe. Samples were packed in a 4 mm zirconium oxide rotor.

### **XAS measurement**

A customized CR2032 coin cell with a hole of 5.0 mm diameter at the center of both cases and spacers was used for all electrochemical tests and transition metal K edge XAS measurements. To assemble the cell, the COF modified Al current collector was cut into a round disk of 10 mm diameter as the examined “working electrode”, and another Zn ring with 6 mm/16 mm inner/outer diameters as the “counter electrode”. GF/A separator (TF4050, NKK Co., Ltd.) with 16.0 mm diameter and 4.0 mm diameter hole at the center was used. 30 μL electrolyte was added. The holes on both sides of the coin cell were sealed by polyamide tape followed by epoxy glue after cell assembly. Cells were rested for 4 h and pre-cycle 1 time to ensure the entrance of Zn ions in COF channel before tests. In situ transition metal K edge XAS were performed at the X-ray Absorption Fine Structure for Catalysis (XAFCA) beamline of Singapore Synchrotron Light Source (SSLS) center. The customized cell was loaded on the sample holder with the polyamide window facing the transmission X-ray pathway. The signal was measured at around 9540 eV for the Zn K edge, respectively, with ~0.9 eV energy step using flying scan mode.

### **Cryo-TEM characterization:**

The crystalline COF powder was first dispersed in ethanol and exposed to ultrasonication treatment for 3 minutes at room temperature. Subsequently, the

dispersion was carefully dropped onto a lacey carbon grid for further investigation using TEM. An aberration-corrected cryogenic TEM operating at a voltage of 300 kV was utilized to characterize the COF specimens at the temperature of liquid nitrogen. All TEM images were captured using a direct-detection electron-counting camera, specifically the Falcon 3, which was controlled by the EPU and Velox software. The measured electron dose for HRTEM was kept below  $100 \text{ e}^- \text{ \AA}^{-2}$ . For collection of Electron Energy Loss Spectroscopy (EELS) spectra and elemental maps, a Gatan Continuum (1069) EELS spectrometer was employed. During the experiment, the beam current was maintained at approximately 50 pA for both the Annular Dark-Field (ADF) imaging and EELS measurement. The spectra and maps were subsequently analyzed and processed using GMS 3 software. The entire experiment was conducted at a low temperature of  $\sim 80 \text{ K}$ , and all HRTEM images were denoised using 3D Wiener filtering.

### **Molecular dynamics simulations**

In this study, the structural properties of  $\text{ZnSO}_4$  solution in COF nanostructures from molecular level are examined by using classic molecular dynamics (MD) simulations. Here, two types of COF nanostructures are taken into investigation for comparison. COF sheets with 2D dimensions of approximately  $60 \times 52 \text{ \AA}^2$  are created, and 6 layered sheets of both COFs are generated, in which 2M  $\text{ZnSO}_4$  solution are randomly placed into the channels of COF sheets. The amount of zinc salt, water applied in this system 60 ( $\text{Zn}^{2+}$  and  $\text{SO}_4^{2-}$ ), 2400 ( $\text{H}_2\text{O}$ ), respectively. 6 layers of COFs are used in this simulation. The COF structure is constructed with supercell of  $2 \times 1 \times 5$ . To remove the effects of boundary surfaces, periodic boundary conditions (PBCs) are imposed in the three orthogonal directions. To describe the atomic interactions in the COF sheets, the Universal Force Field for Metal–Organic Frameworks (UFF4MOF) is utilized<sup>1</sup>, in which the atomic charges of COF sheets are assigned based on the repeating electrostatic potential extracted atomic charge method (REPEAT) method<sup>2</sup>. To describe the non-bonded interactions, the van der Waals (vdW) interactions are considered by the Lennard-Jones 12-6 potential with a cut-off distance of  $10 \text{ \AA}$ , while the long-range

electrostatic interactions are described by the standard Coulomb potential via the particle-particle-particle-mesh (PPPM) algorithm. Prior to MD simulations, all COF-based systems are geometrically minimized to a local configuration with energy and force tolerances of  $1.0 \times 10^{-4}$  Kcal/mol and  $1.0 \times 10^{-4}$  Kcal/(mol·Å), respectively. Afterwards, MD simulations with 1,000,000 timesteps are performed to relax the systems at temperature of 300 K under canonical ensemble (NVT). Finally, MD simulations with another 1,000,000 timesteps are carried out to capture the structural properties for as-investigated systems. It is noted that the backbones of COF sheets are frozen during the entire MD simulations. The timestep is set as 1.0 fs. All the MD simulations are implemented using the Large-scale Atomic/Molecular Massively Parallel Simulator (LAMMPS) package<sup>3</sup>. Note that there are no differences in the initial state of electrolyte in the cross-sectional areas in any system, as demonstrated in Figures S23 and S24. Any observed variations in the horizontal direction are due to the interactions between different COFs and the electrolyte.

The PFM was conducted in this study utilized the GROMACS 2023.2 package. The GAFF force field and TIP3P water model were employed, with a cut-off of 1.0 nm for electrostatic and van der Waals interactions. Long-range electrostatic interactions were calculated using the particle mesh Ewald (PME) summation method. A universal time step of 1 fs was used in all simulations. The SHCOF systems comprised approximately 16,000 atoms within boundaries of  $6.02 \times 5.22 \times 5.47$  nm<sup>3</sup>, while the SPCOF systems comprised approximately 17,000 atoms within boundaries of  $5.88 \times 5.09 \times 5.86$  nm<sup>3</sup>. Initial structures were built based on COF crystal data, incorporating 5,000 water molecules, 1 Zn<sup>2+</sup> ion, and 1 SO<sub>4</sub><sup>2-</sup> ions to ensure charge neutrality. For each system, energy minimization and NpT ensemble equilibration procedures were initially performed to obtain equilibrated structures. Subsequently, NVT ensemble COM-pulling procedures were applied to generate sampling windows for potential of mean force (PMF) calculations. In this procedure, the reaction coordinates were defined as the distance between the Zn<sup>2+</sup> ion and the mass center of the COF membranes. A harmonic umbrella potential with a strength of 3000 kJ mol<sup>-1</sup> nm<sup>-2</sup> was applied to drive the Zn<sup>2+</sup> ion along the reaction pathway from -0.6 nm to 0.6 nm, covering 0.6 nm before

entering the membrane zone and 0.6 nm after exiting the membrane zone. During this step, 100 parallel sampling windows were generated for each system. Finally, all sampling windows were run for 2 ns equilibration followed by 10 ns sampling, with the  $\text{Zn}^{2+}$  ion constrained at specific positions along the reaction pathway by the harmonic umbrella potential of  $3000 \text{ kJ mol}^{-1} \text{ nm}^{-2}$  strength. Data on reaction coordinates and forces obtained from the 10 ns sampling were aggregated to calculate the final PMF profiles using the Weighted Histogram Analysis Method (WHAM) module in GROMACS.

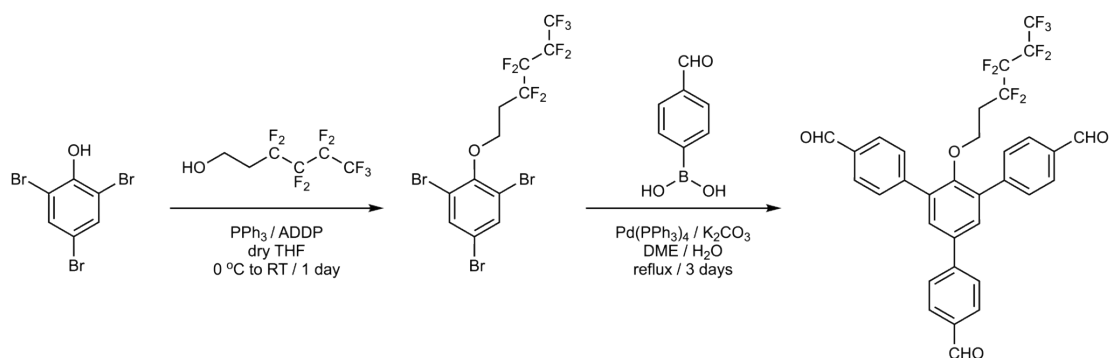


**Figure S1.** Synthesis process of 5'-(4-formylphenyl)-2'-((3,3,4,4,5,5,6,6,6-nonafluorohexyl)oxy)-[1,1':3',1''-terphenyl]-4,4''-dicarb-aldehyde (TFPBPFHex)

A solution of 2,4,6-tribromophenol (3.3 g, 10 mmol) was prepared in anhydrous tetrahydrofuran (THF) (20 mL) alongside triphenylphosphine (5.24 g, 20 mmol) and 1,1'-(azodicarbonyl)dipiperidine (ADDP) (5.04 g, 20 mmol). To this mixture, 1H,1H,2H,2H-perfluorohexan-1-ol (12 mmol, 1.994 mL) was added at a controlled temperature of 0 °C under an argon atmosphere. The mixture was then allowed to warm to room temperature and was continuously stirred for 24 hours to complete the reaction phase. Post-reaction, the mixture was evaporated under vacuum to remove the solvent. The crude residue obtained was subjected to column chromatography using hexane to elute the product, resulting in a colorless oil. This oil was then dissolved in a mixture prepared from 4-formylphenylboronic acid (5.1 g, 24 mmol), palladium tetrakis(triphenylphosphine) (200 mg, 0.184 mmol), and potassium carbonate (16.6 g, 120 mmol) in a solution of dimethoxyethane (DME) and water (80 mL, v/v = 3:1). This reaction mixture was heated at reflux under an argon atmosphere for three days. After cooling to room temperature, the reaction mixture was filtered through a Celite bed to remove particulates. The filtrate was then subjected to extraction with dichloromethane (four times), and the organic layers obtained from this step were combined and dried over sodium sulfate. The solvent from the combined organic layers was removed under vacuum. The resultant residue was further purified by silica gel column chromatography using a hexane/ethyl acetate mixture (v/v = 10:1) as the eluent. The final product was a white crystalline solid (3.1 g, 47.5% yield over two steps). <sup>1</sup>H NMR (400 MHz, CDCl<sub>3</sub>) δ 10.09 (d, *J* = 12.5 Hz, 3H), 8.00 (dd, *J* = 10.3, 8.4 Hz, 6H), 7.83

(dd,  $J = 14.0, 8.2$  Hz, 6H), 7.68 (d,  $J = 4.1$  Hz, 2H), 3.53 (t,  $J = 6.7$  Hz, 2H), 1.96 (tt,  $J = 18.5, 6.6$  Hz, 2H). APCI-HRMS Calcd. For [C<sub>33</sub>H<sub>22</sub>F<sub>9</sub>O<sub>8</sub>] 653.1369, found 653.1368.

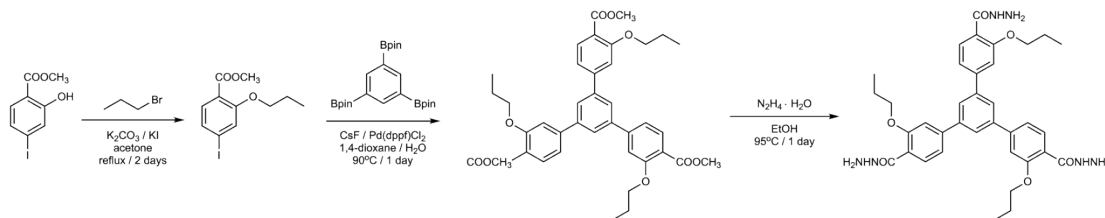


**Figure S2.** Synthesis process of 5'-(4-(Hydrazinecarbonyl)-3-propoxyphenyl)-3,3'-dipropoxy-[1,1':3',1''-terphenyl]-4,4''-dicarbohydrazide (THzOPr)

Methyl 2-hydroxy-4-iodobenzoate (2.78 g, 10 mmol), K<sub>2</sub>CO<sub>3</sub> (5.6 g, 40 mmol), and KI (100 mg, 0.6 mmol) were dissolved in acetone (150 mL). To this mixture, 1-propylbromide (2 mL, 22 mmol) was added dropwise. The solution was refluxed under a nitrogen atmosphere for 2 days and subsequently hot-filtered through a Celite bed. The filtrate was evaporated and the residue underwent flash chromatography (hexane/ethyl acetate = 5:1) to yield a colorless oil. 1.28 g of this product was then reacted with 1,3,5-Tris(4,4,5,5-tetramethyl-1,3,2-dioxaborolan-2-yl)benzene (456 mg, 1 mmol), cesium fluoride (1.35 g, 8.9 mmol), and Pd(dppf)Cl<sub>2</sub> (80 mg, 0.1 mmol) in the mixture of 1,4-dioxane (12 mL) and water (12 mL) under nitrogen at 90 °C for 1 day. After cooling, the mix was diluted with ethyl acetate and water. The organic layer was separated, washed with brine, dried over Na<sub>2</sub>SO<sub>4</sub>, and evaporated. Final purification via flash chromatography (hexane/ethyl = 10:1 then CH<sub>2</sub>Cl<sub>2</sub>) yielded a white solid product (558 mg, 85% yield). The product was then suspended in ethanol (10 mL) and treated with hydrazine monohydrate (1.5 mL). After stirring at 95 °C for 1 day and cooling down, the product was filtered, washed with cold ethanol, and dried to yield a white solid (446 mg, 80%). <sup>1</sup>H NMR (500 MHz, DMSO) δ 9.15 (s, 3H), 8.00 (s, 3H), 7.86 (d,  $J = 7.9$  Hz, 3H), 7.53 (d,  $J = 9.6$  Hz, 6H), 4.59 (s, 6H), 4.25 (t,  $J = 6.4$  Hz, 7H), 1.83 (dd,  $J = 14.0, 6.8$  Hz, 6H), 1.03 (t,  $J = 7.4$  Hz, 9H). <sup>13</sup>C NMR (126 MHz, DMSO) δ 165.55, 157.60, 144.70, 141.91, 131.76, 126.57, 122.24, 120.51, 112.87,

71.14, 22.84, 11.44. ESIHRMS Calcd. for [C<sub>36</sub>H<sub>43</sub>N<sub>6</sub>O<sub>6</sub>+H] 655.3239, found 655.3234.

**Synthesis of SPCOF and SHCOF:**

For SPCOF: TFPBPFHex (13 mg, 0.02mmol) and THzOPr (13.1 mg, 0.02mmol) were added into a 10mL Schlenk tube (15 mm × 80 mm) followed by the addition of o-DCB (0.25 ml) and mesitylene (0.75 ml). The mixture was sonicated for 3 min before acetic acid (6 M, 0.1 ml) was added, which was then flash frozen at 77 K and degassed by freeze-pump-thaw for three times. The tube was sealed and heated at 120 °C for three days. The solid was collected by filtration and washed with THF (5 ml) three times and dichloromethane (5 ml) two times to give a white solid (30.8 mg, 82%).

For SHCOF: TFPB was purchased from TCI. TFPB (7.8 mg, 0.02 mmol) and THzOPr (13.1 mg, 0.02 mmol) were added into a 10mL Schlenk tube (15 mm × 80 mm) followed by the addition of mesitylene (0.5 ml) and 1,4-dioxane (0.5 ml). The mixture was sonicated for 3 min before acetic acid (6 M, 0.1 ml) was added, which was then flash frozen at 77 K and degassed by freeze-pump-thaw for three times. The tube was sealed and heated at 120 °C for three days. The solid was collected by filtration and washed with THF (5 ml) three times and dichloromethane (5 ml) two times to give a white solid (18.9 mg, 95%).

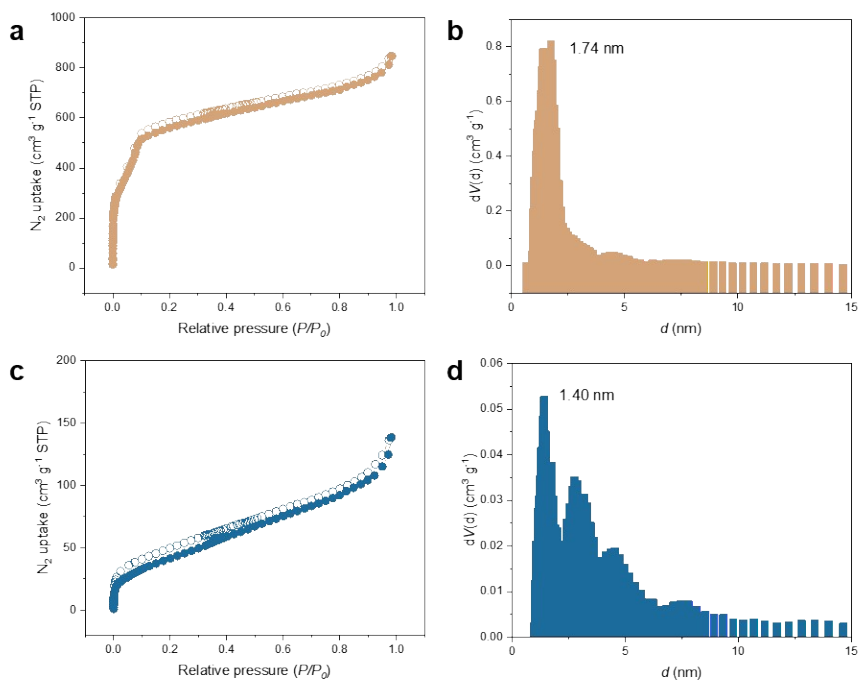


**Figure S3.** N<sub>2</sub> adsorption-desorption isotherms (77 K) of SPCOF and SHCOF. (a, b) SHCOF. (c, d) SPCOF. The surface areas of SPCOF and SHCOF calculated by N<sub>2</sub> adsorption-desorption isotherms are 1421 m<sup>2</sup> g<sup>-1</sup> and 106 m<sup>2</sup> g<sup>-1</sup>, respectively.

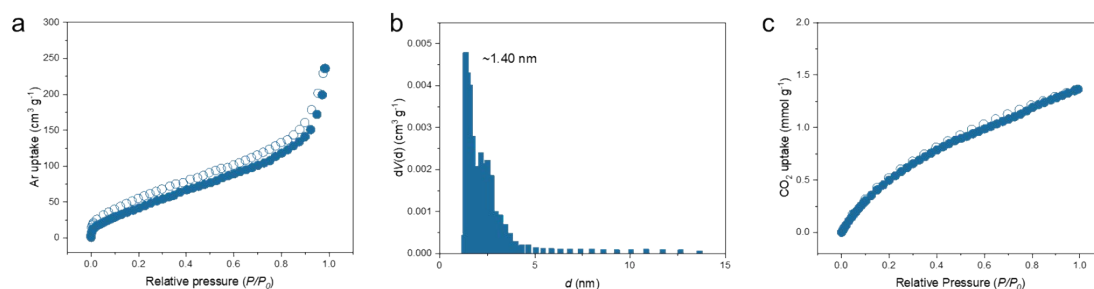


**Figure S4.** Ar adsorption-desorption isotherm (a) and pore size distribution (b) of SPCOF (87 K), CO<sub>2</sub> adsorption-desorption isotherm (c) of SPCOF (273K). The BET surface area of SPCOF calculated by Ar adsorption-desorption isotherms is 121 m<sup>2</sup> g<sup>-1</sup>.

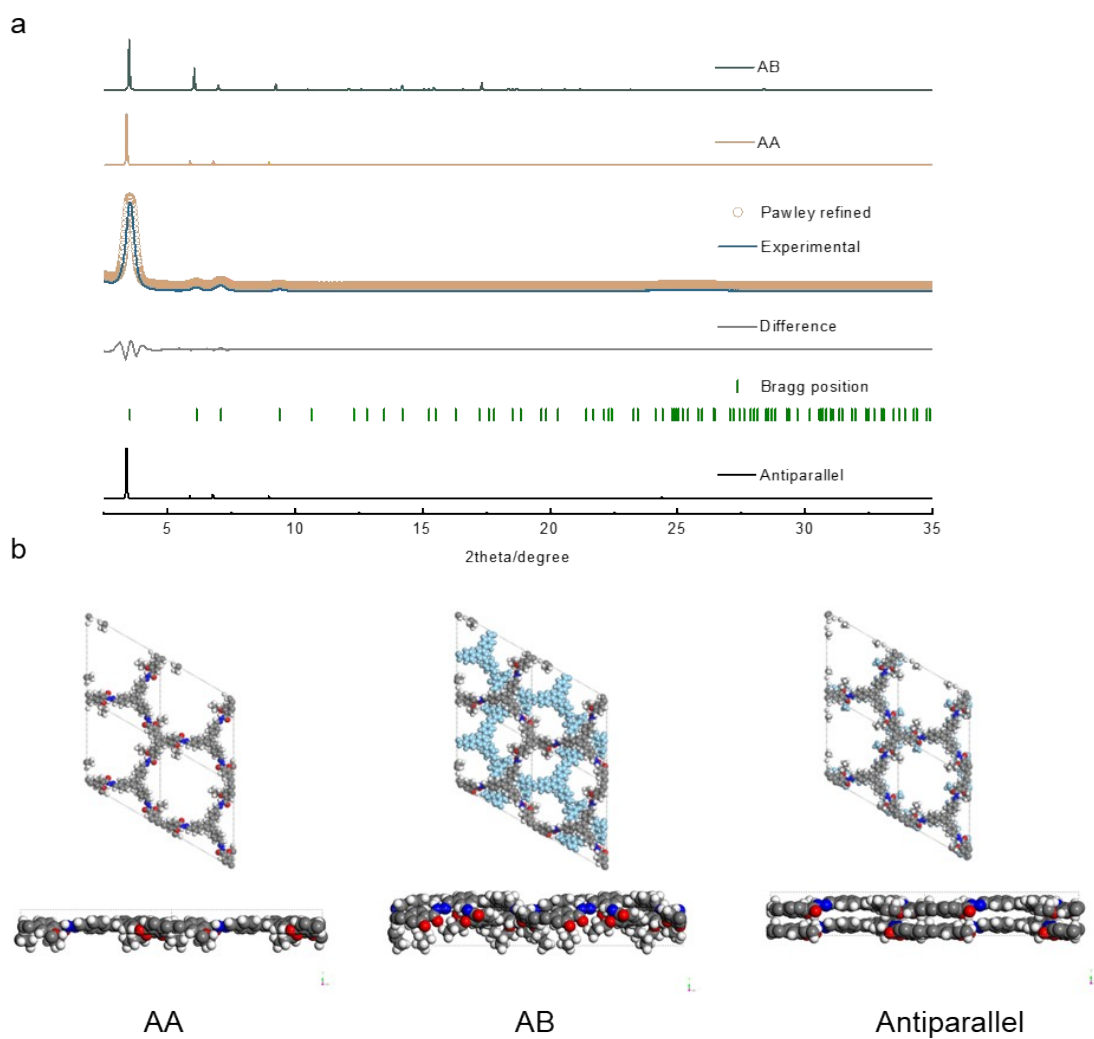


**Figure S5.** Structural determination of SHCOF. (a) PXR D patterns of SHCOF (experimental: black; Pawley refined: red; Difference: grey; simulated antiparallel stacking: green; simulated eclipsed stacking: purple; simulated staggered stacking: yellow). (b) Pawley-refined structures of antiparallel stacking, eclipsed (AA) stacking, and staggered (AB) stacking.

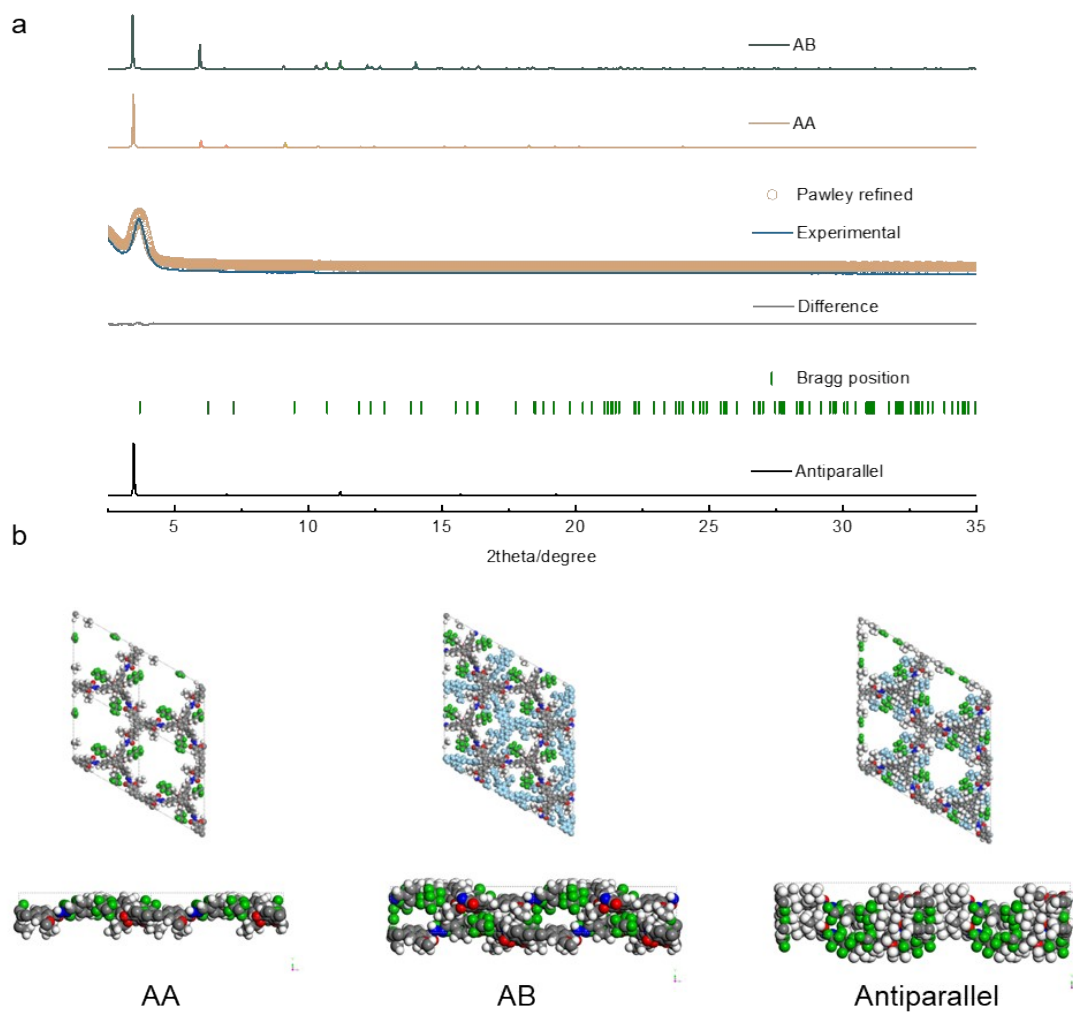


**Figure S6.** Structural determination of SPCOF. (a) PXRD patterns of SPCOF (experimental: black; Pawley refined: red; Difference: grey; simulated antiparallel stacking: green; simulated eclipsed stacking: purple; simulated staggered stacking: yellow). (b) Pawley-refined structures of antiparallel stacking, eclipsed stacking, and staggered stacking.

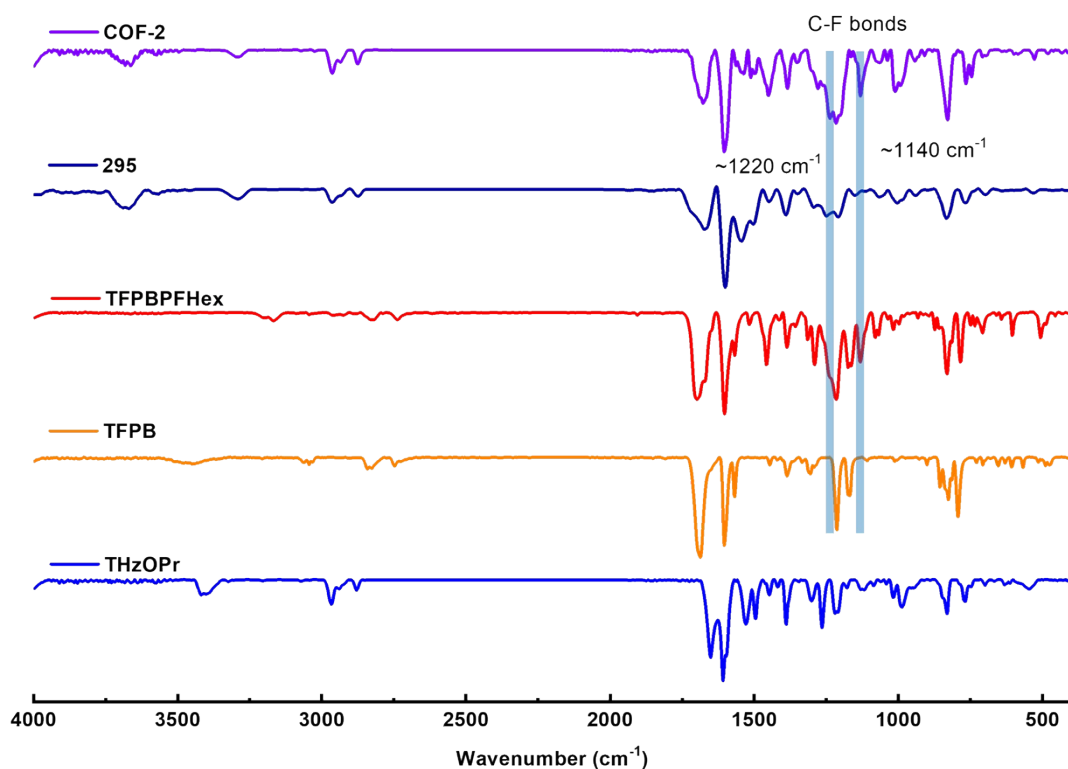


**Figure S7.** FT-IR spectra of as synthesized COFs and their building units.

The peaks at  $\sim 1220\text{ cm}^{-1}$  and  $\sim 1140\text{ cm}^{-1}$  can be assigned to typical C-F bonding<sup>4,5</sup>. (Analytical chemistry, 2016, 88(7): 3926-3934; Physical Chemistry Chemical Physics, 2021, 23(47): 26853-26863).

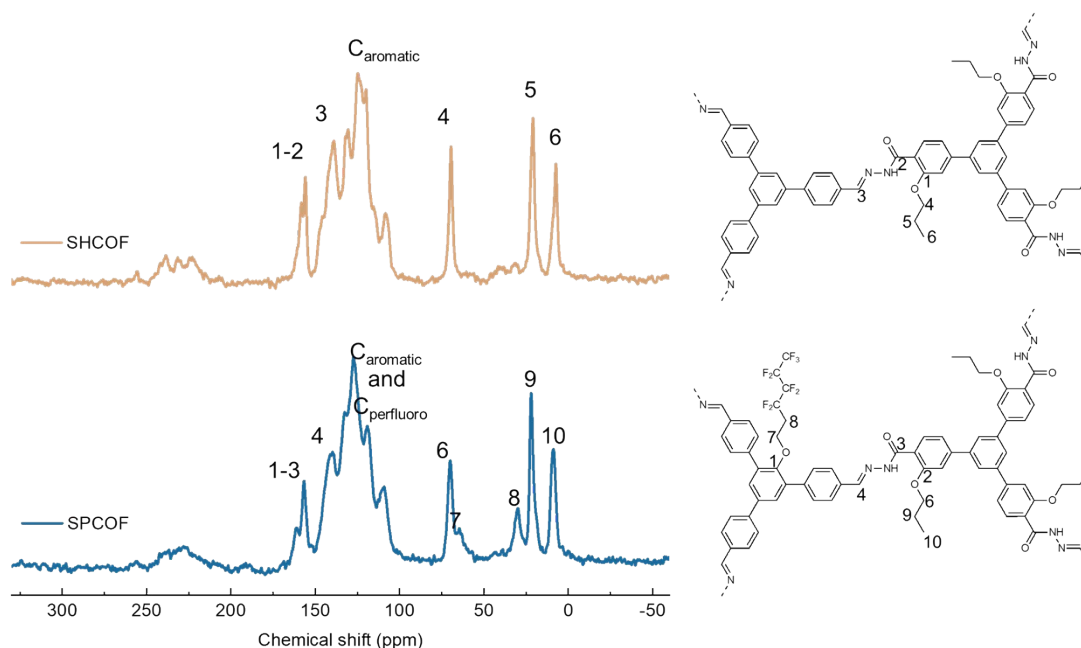


**Figure S8.** Solid-state CP/MAS  $^{13}\text{C}$  NMR spectra of as synthesized COFs.

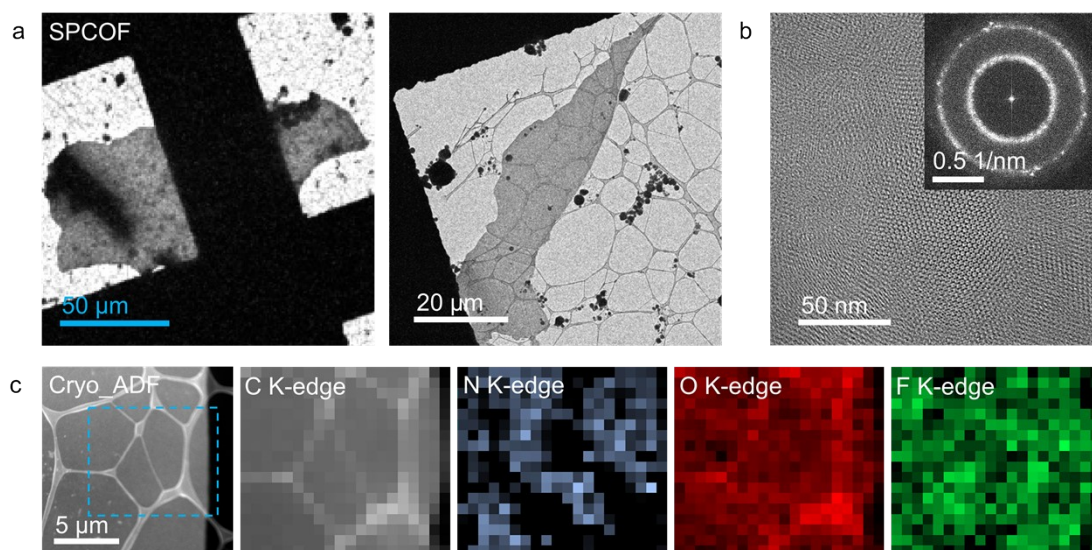


**Figure S9.** Morphological images and elemental maps of SPCOF. (a) Low-magnification TEM images of SPCOF obtained by solvent-assisted ultrasonic exfoliation. (b) Large-scale, high-resolution Cryo-TEM image of FCOF and its fast Fourier transform (FFT) pattern. (c) Cryo-ADF STEM image and EELS elemental maps of C, N, O and F from the blue dashed-line box region

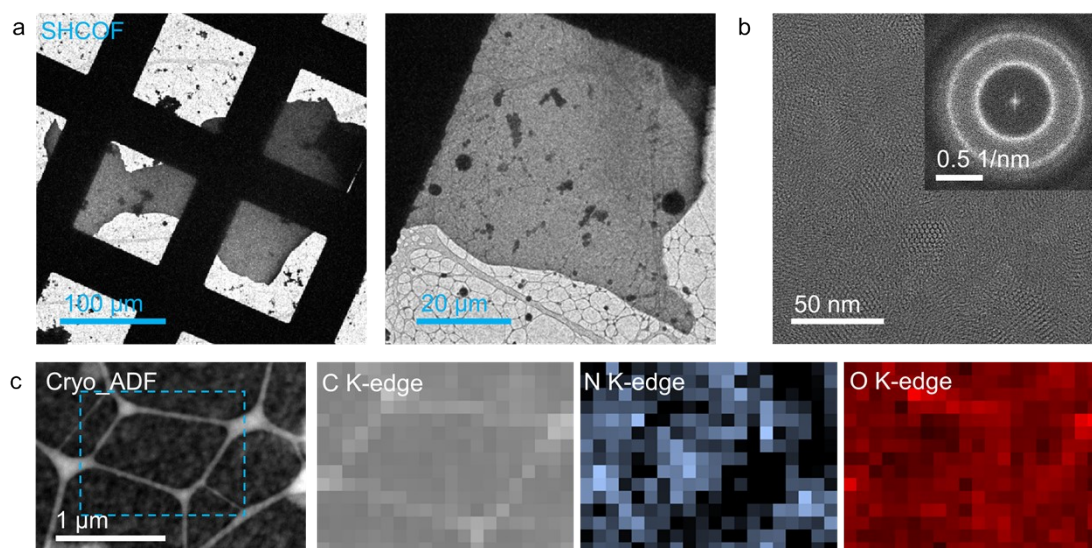


**Figure S10.** Morphological images and elemental maps of SHCOF. (a) Low-magnification TEM images of SHCOF obtained by solvent-assisted ultrasonic exfoliation. (b) Large-scale, high-resolution Cryo-TEM image of CCOF and its FFT pattern. (c) Cryo-ADF STEM image and EELS elemental maps of C, N and O from the blue dashed-line box region.

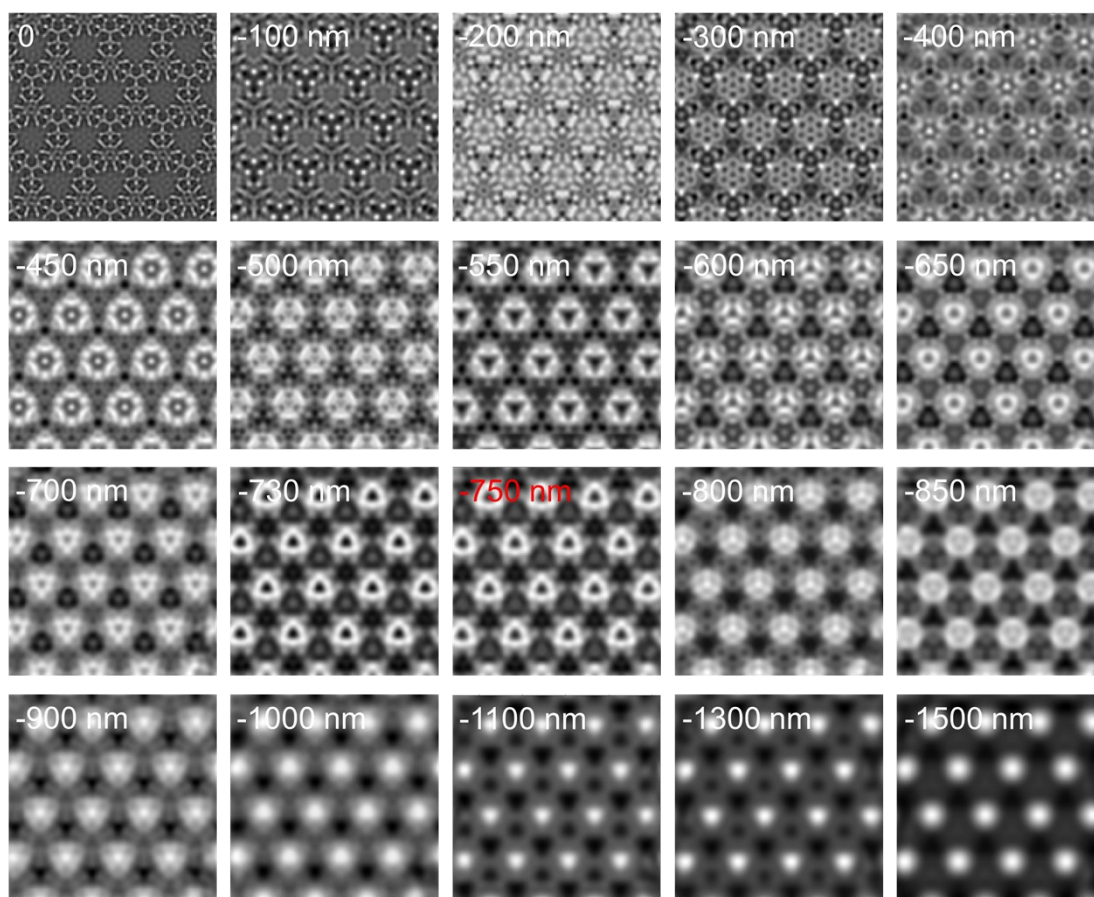


**Figure S11.** Simulated HRTEM images of SPCOF along the [001] direction using the multi-slice method at varying defocus values.

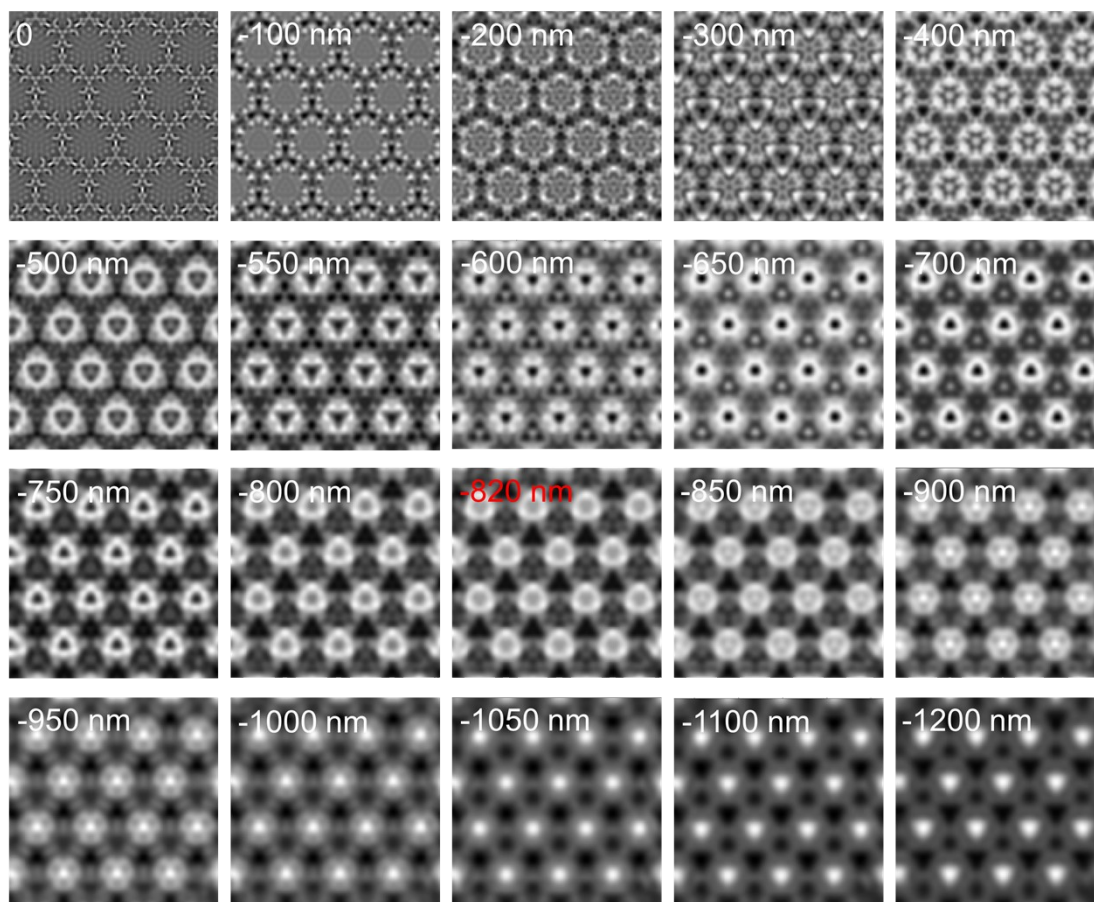


**Figure S12.** Simulated HRTEM images of SHCOF along the [001] direction using the multi-slice method at varying defocus values.

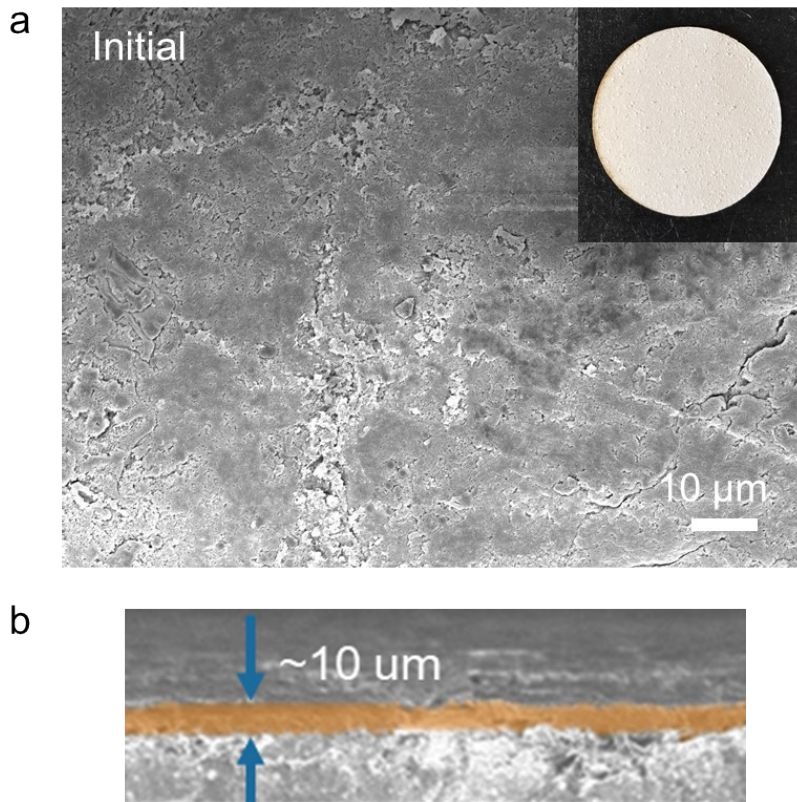


**Figure S13.** SEM images of SPCOF@Zn: (a) top view and (b) cross section view.

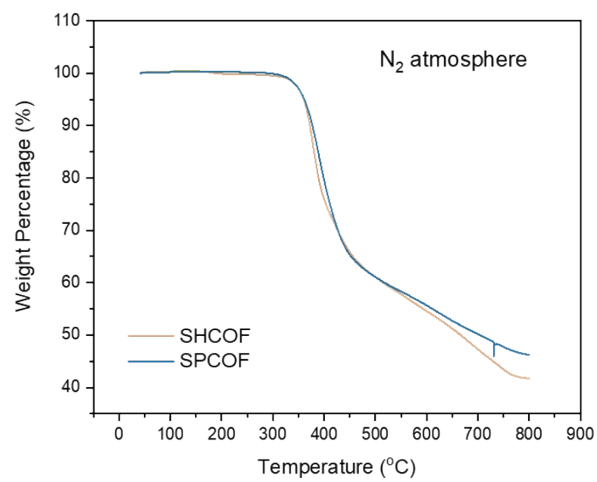


**Figure S14.** TGA curves of SHCOF and SPCOF.



**Figure S15.** 2D Raman mapping on the surfaces of bare Zn (a), SHCOF@Zn (b) and SPCOF@Zn(c) after immersion in electrolyte for 7 days. insets show images of the interfaces between various electrodes and electrolyte, with the electrolyte visualized using methyl blue staining, scale bar: 10 um.

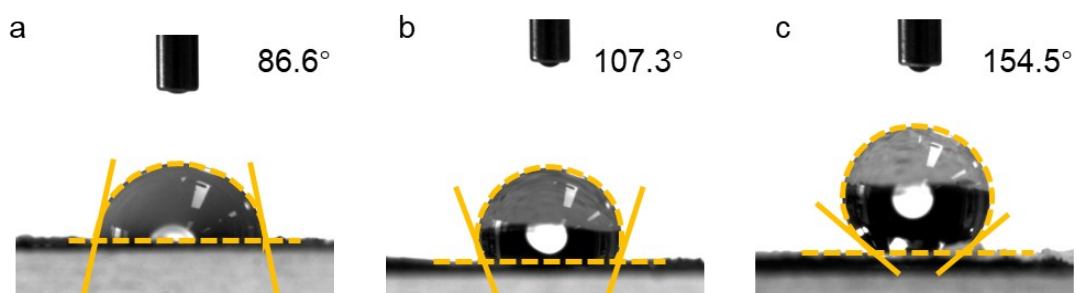


**Figure S16.** Contact angles between electrolyte and different electrode: (a) SPCOF@Zn, (b) SHCOF@Zn and (c) bare Zn

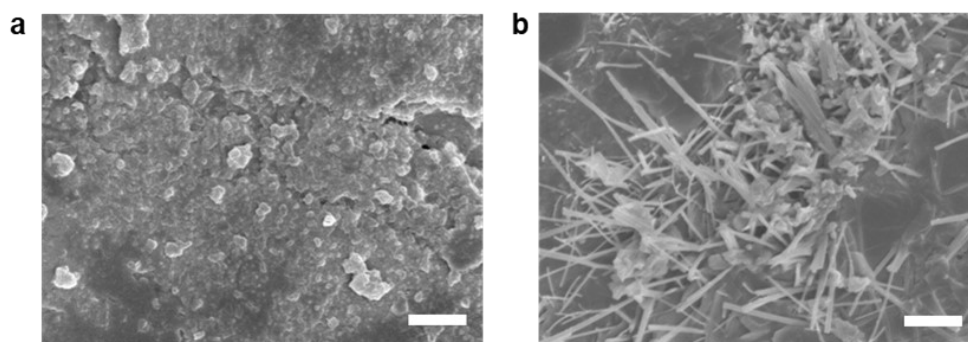


**Figure S17.** SEM images of bare Zn before (a) and after (b) immersion in electrolyte for 7 days.

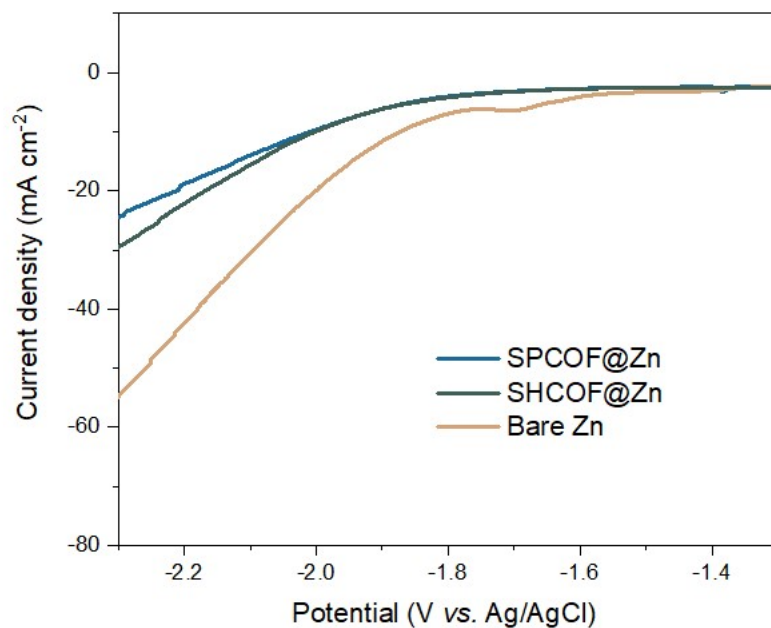


**Figure S18.** Linear sweep voltammetry (LSV) curves obtained using a 1M aqueous  $\text{Na}_2\text{SO}_4$  solution as the electrolyte, with a scan speed of  $5\text{mV s}^{-1}$ .

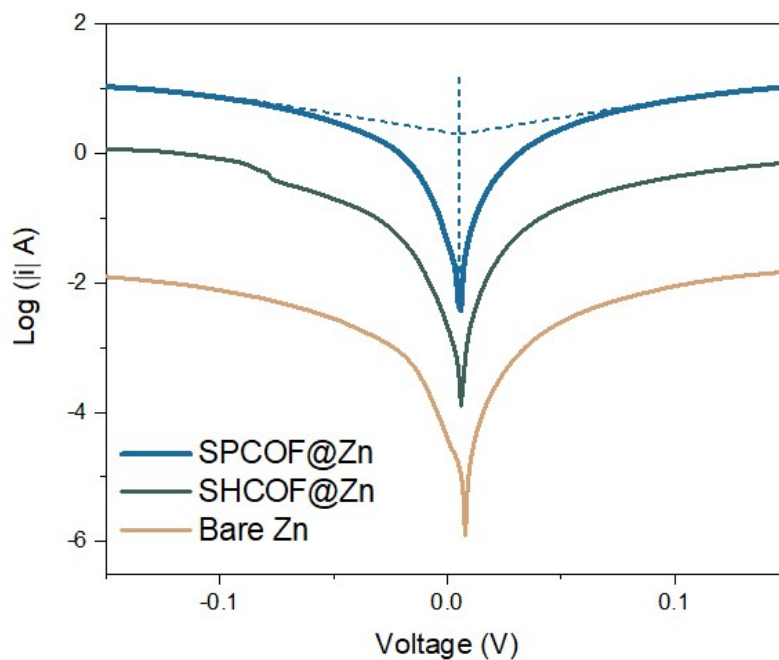


**Figure S19.** Tafel plots illustrating the corrosion behavior of Zn anodes in a 2M aqueous  $\text{ZnSO}_4$  electrolyte.

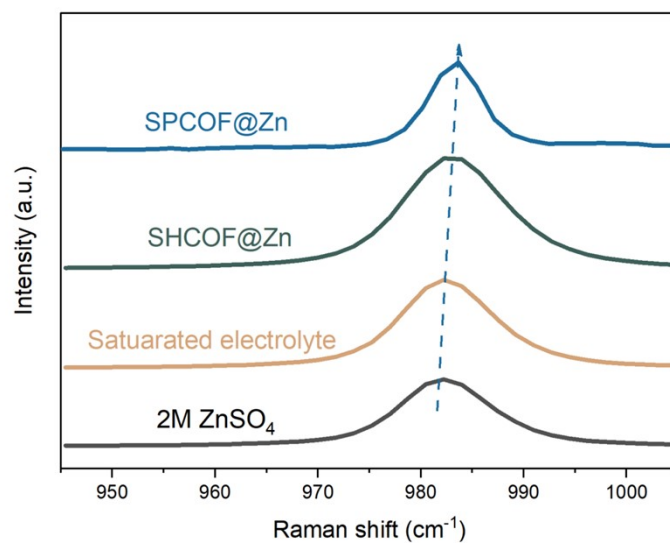


**Figure S20.** Raman spectra showcasing electrolytes with different concentration and within SPCOF/SHCOF channels.

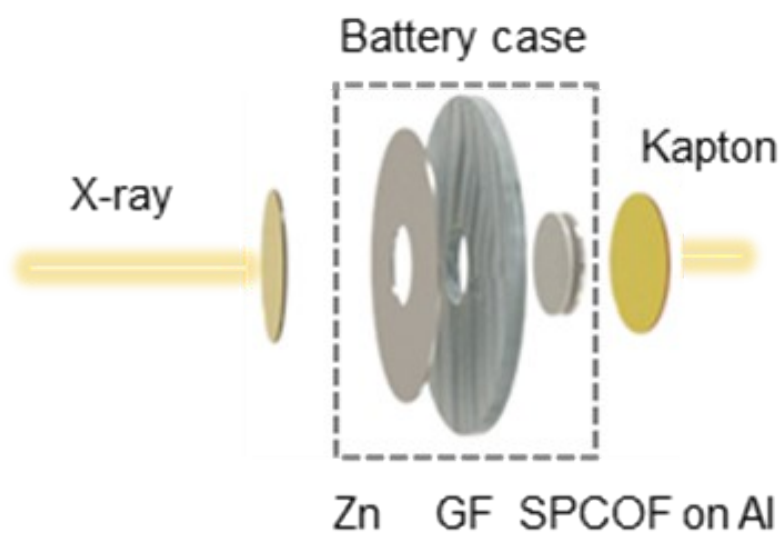


**Figure S21.** Illustration showing the setup of XAS tests.

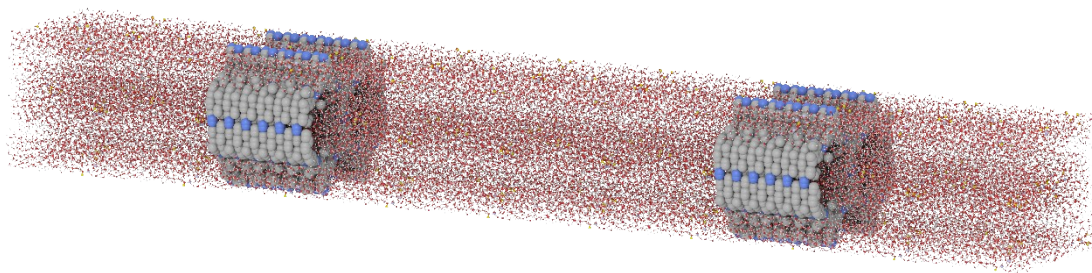


**Figure S22.** Models of the MD simulations of SPCOF-2M ZnSO<sub>4</sub>.

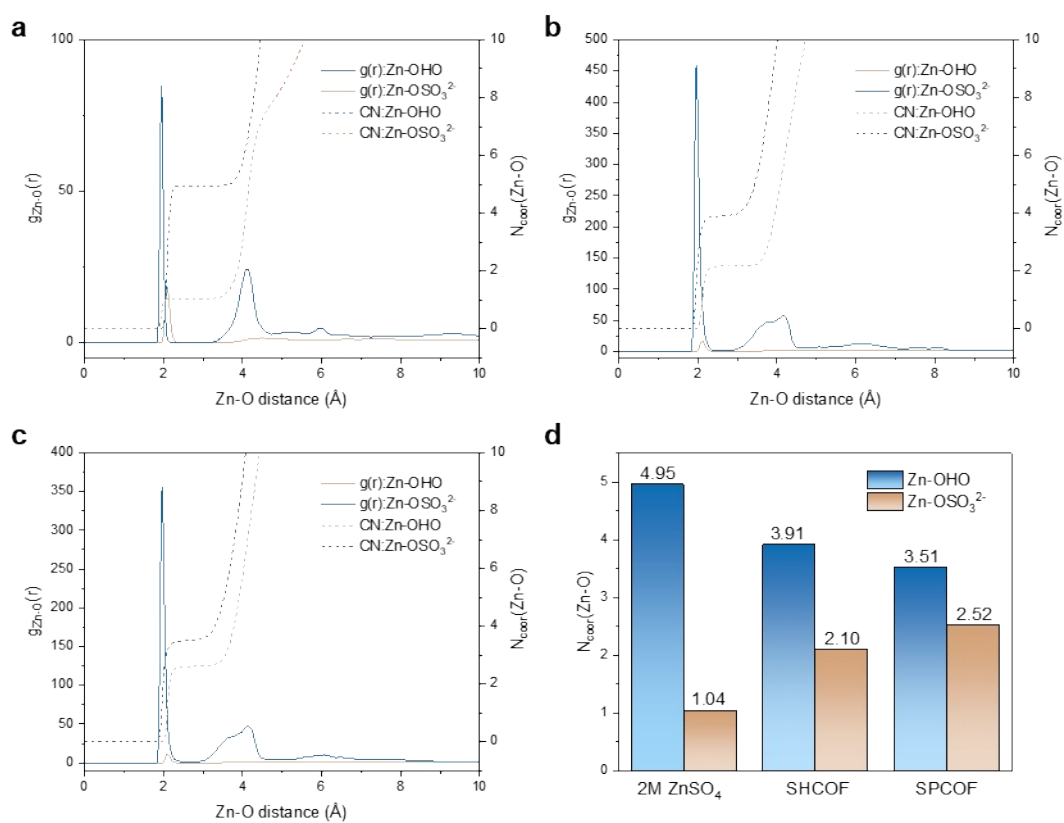


**Figure S23.** RDF and coordination number of zinc ion and oxygen in (a) 2M ZnSO<sub>4</sub> solution, (b) SHCOF confined electrolyte, and (c) SPCOF confined electrolyte.

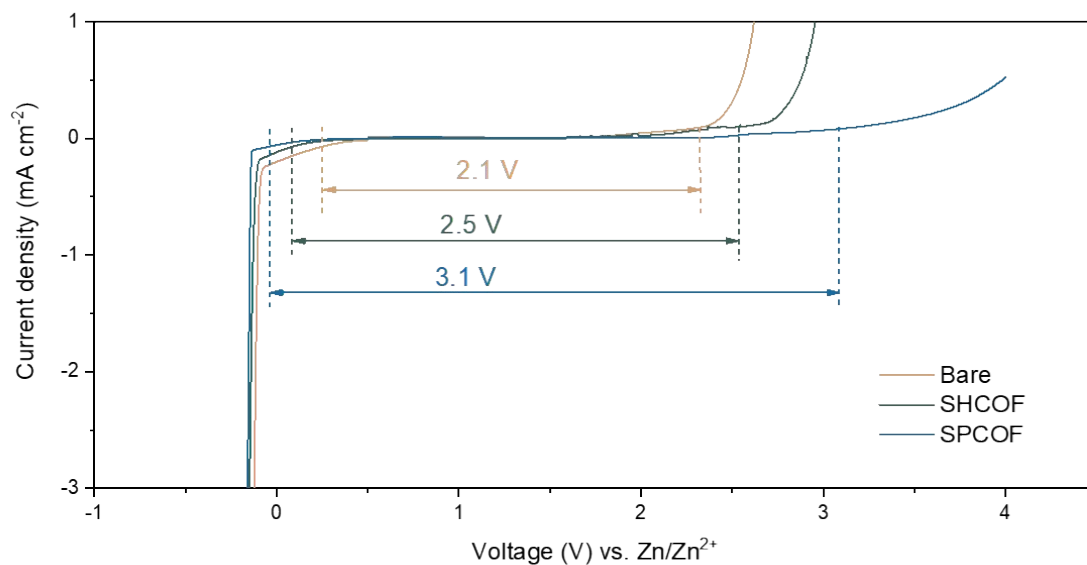


**Figure S24.** LSV curves of Zn-Ti batteries showcasing the voltage windows of various electrodes in a 2M aqueous ZnSO<sub>4</sub> electrolyte

**Notes for Figure S24:**

The ESW were tested by Zn-Ti batteries in a 2M aqueous ZnSO<sub>4</sub> electrolyte. Zn and Ti foil were served as reference and working electrodes, respectively. It can be seen that the introduction of SPCOF layer can expand the ESW efficiently. This can be attributed to be attributed to the superhydrophobic nature and rapid dehydration process facilitated by the SPCOF layer. These properties reduce the presence of free water and decrease the reactivity of the electrolyte near the zinc surface, as noted in previous studies<sup>6,7</sup>. This effect is further supported by the in-situ gas chromatography (GC) test presented in Figure 4a.

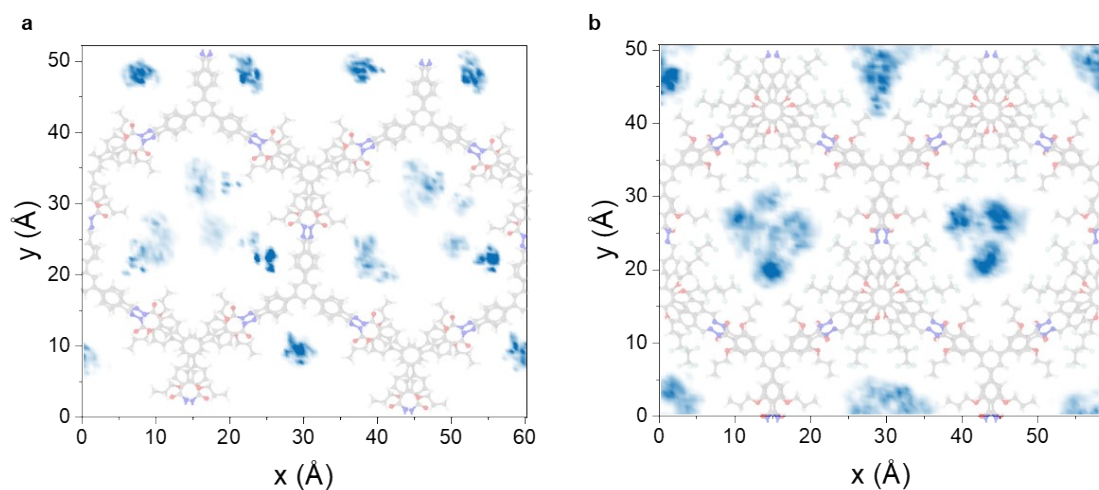


**Figure S25.** 2D density contour displaying the distribution of  $\text{SO}_4^{2-}$  different COF channels: (a) SHCOF, (b) SPCOF

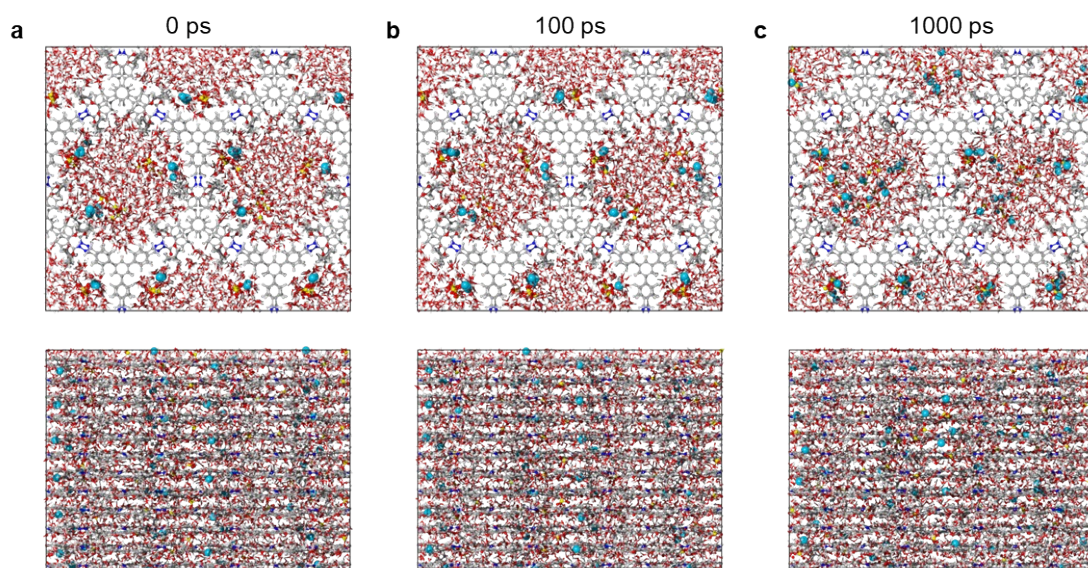


**Figure S26.** Atomic configuration and local density of electrolytes in SHCOF at the different times (0 ps, 100 ps and 1000 ps) during simulations, the blue ball represents SH atoms in the system.

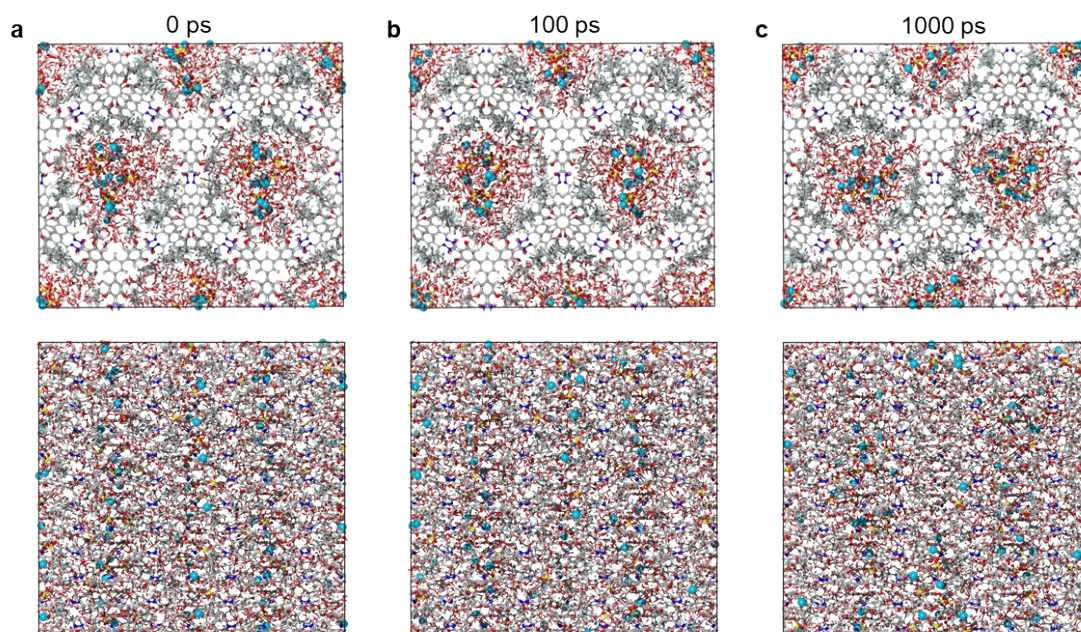


**Figure S27.** Atomic configuration and local density of electrolytes in SPCOF at the different times (0 ps, 100 ps and 1000 ps) during simulations, the blue ball represents Zn atoms in the system.

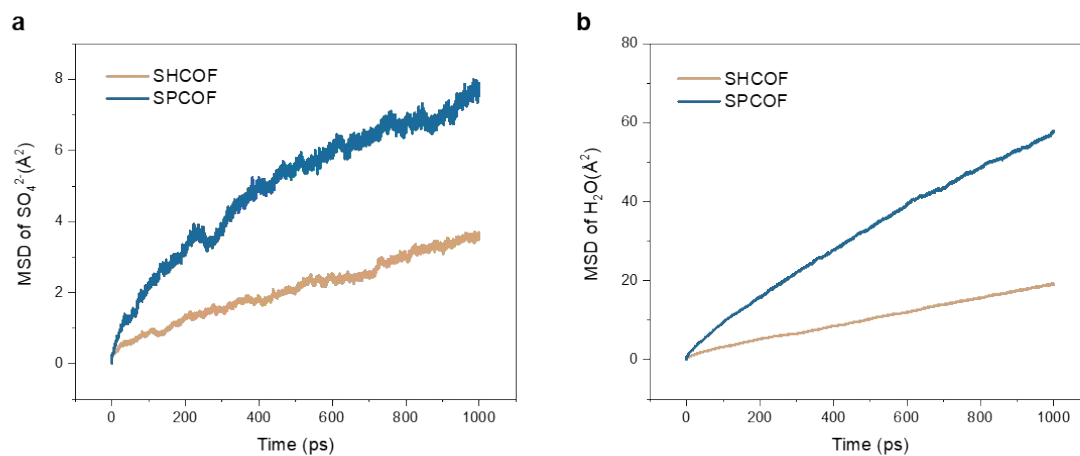


**Figure S28.** MSD of SO<sub>4</sub><sup>2-</sup> (a) and H<sub>2</sub>O (b) within the SPCOF channel and SHCOF channel

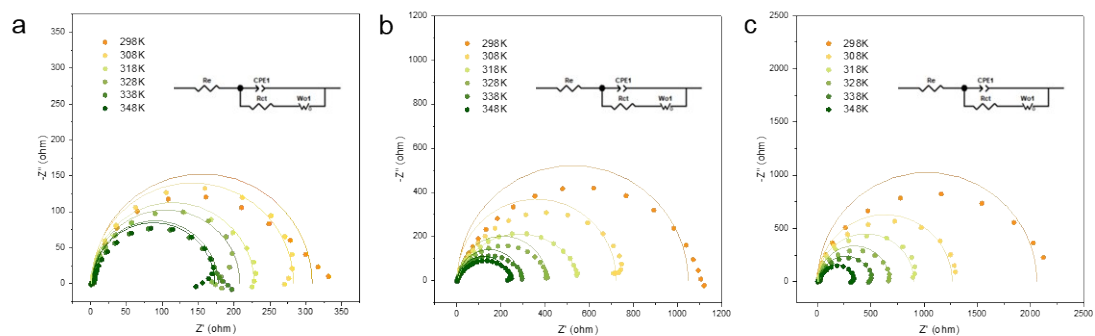


**Figure S29.** Nyquist plots and the corresponding fitting curves of Zn symmetric cells at various temperatures ranging from 298K to 348K: (a) SPCOF@Zn, (b) SHCOF@Zn, (c) bare Zn.

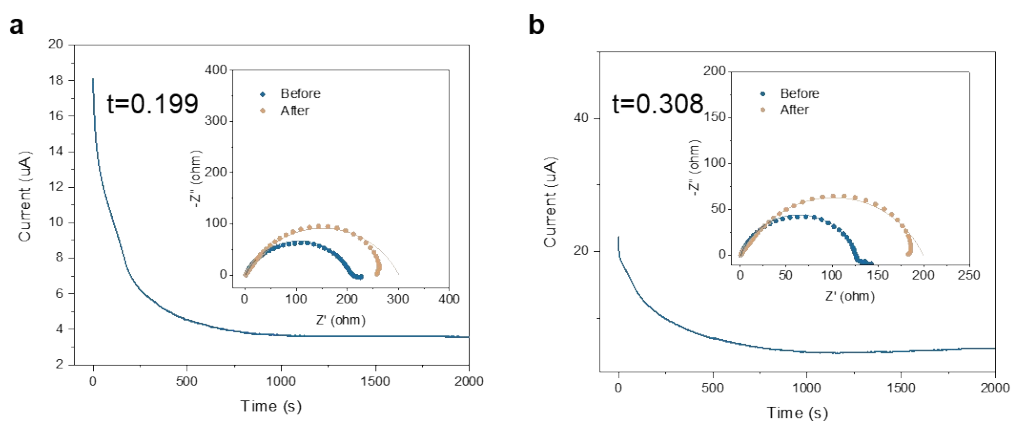


**Figure S30.** Current-time curves of Zn symmetric cells following a constant polarization of 10 mV for 1500 s with SHCOF@Zn (a) and bare Zn (b). Inset: Electrochemical impedance spectroscopy (EIS) result of the Zn symmetric cell before and after the transference number test.

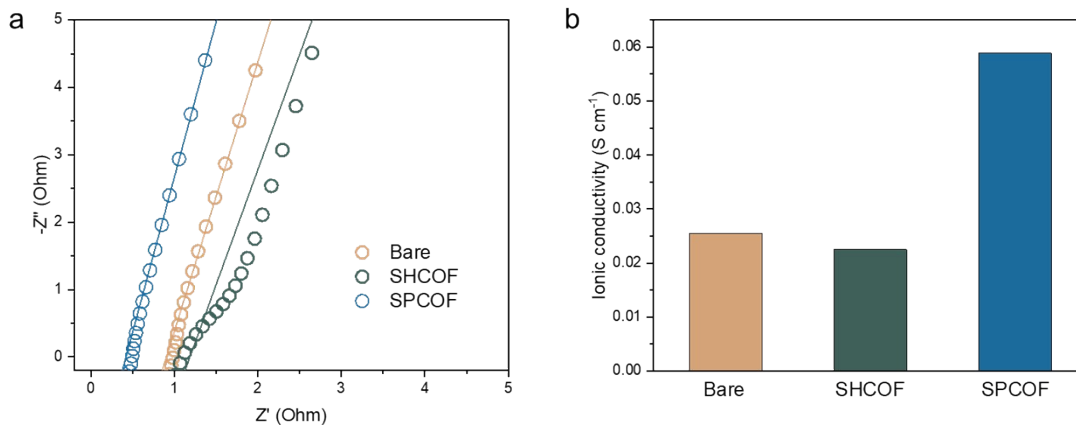


**Figure S31.** (a) EIS results of symmetric cells in bare Ti//bare Ti, SHCOF@Ti//SHCOF@Ti, and SPCOF@Ti//SPCOF@Ti configurations (immersed in 2M ZnSO<sub>4</sub>). (b) Calculated ionic conductivity based on the EIS results.

**Note for Figure S29:**

The ionic conductivity can be obtained from  $R_s$  by the following equation:

$$\sigma = \frac{L}{R_s S} \quad \text{Equation 1}$$

where  $\sigma$  is the ionic conductivity,  $L$  is the Zn ion diffusion distance.  $R_s$  and  $S$  are the electrolyte resistance and electrode surface, respectively.

The ionic conductivity of SPCOF reached 0.0589 S cm<sup>-1</sup>, which is higher than that of SHCOF (0.0225 S cm<sup>-1</sup>) and GF/D separator (0.0255 S cm<sup>-1</sup>).

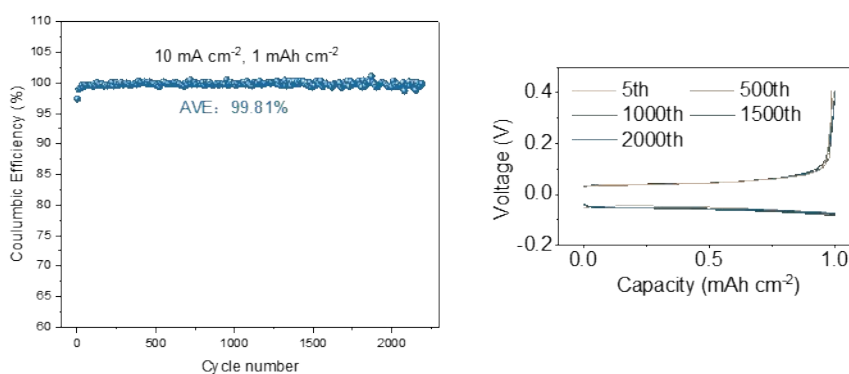


**Figure S32.** Galvanostatic Zn stripping/plating behavior in Zn||Zn symmetric cells with different modification layers at 10 mA cm<sup>-2</sup> with a 1 mAh cm<sup>-2</sup> capacity and corresponding galvanostatic charge-discharge profiles at different cycles.

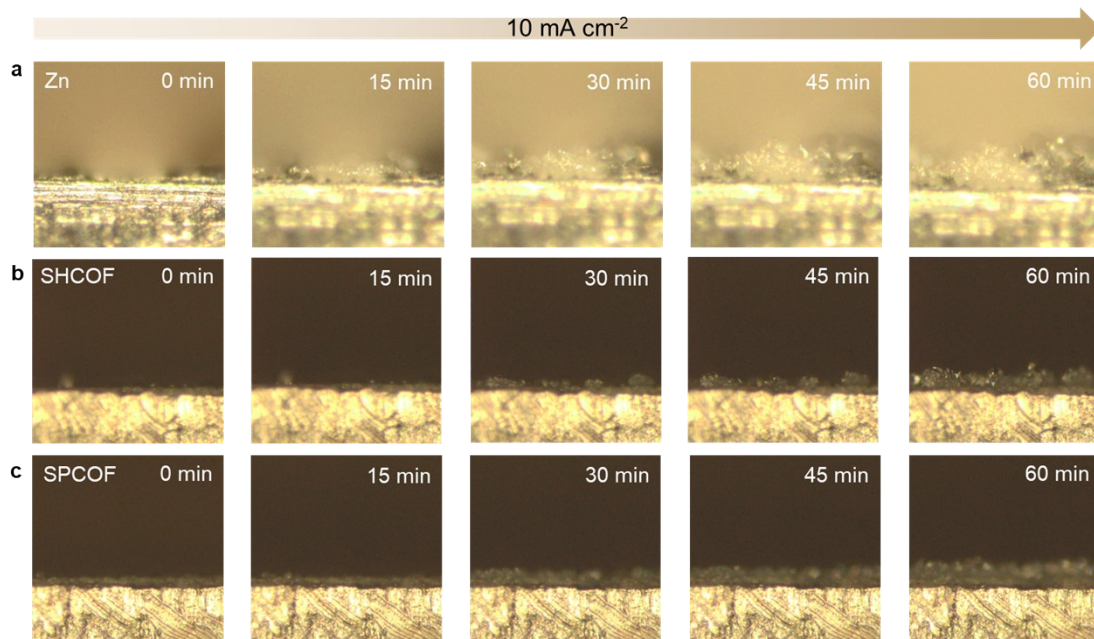


**Figure S33.** In situ optical observations of Zn electrodeposition on bare Zn (a), SHCOF@Zn (b), and SPCOF@Zn anodes

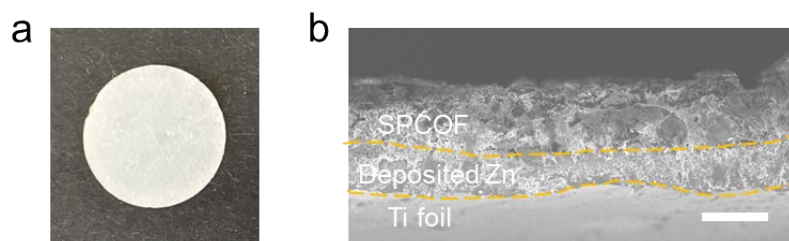


**Figure S34.** Digital photos (a) and cross-sectional view SEM images (b) of the SPCOF@Ti electrode following Zn deposition. The capacity was recorded at 1 mAh cm<sup>-2</sup> at a current density of 1 mA cm<sup>-2</sup> (scale bar: 10 μm).

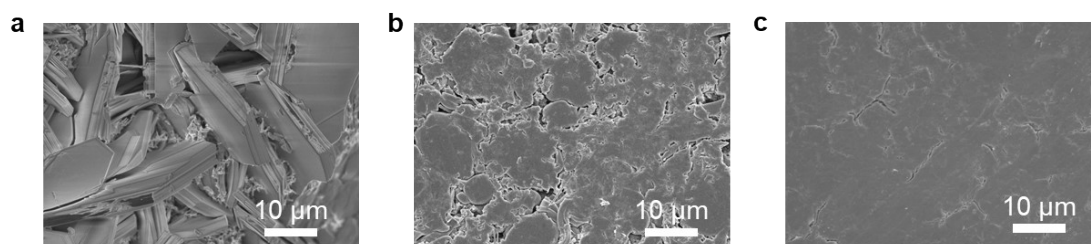


**Figure S35.** Morphology of deposited Zn on bare Zn (a), SHCOF@Zn (b) and SPCOF@Zn (c) electrodes. The deposition current is 1 mA cm<sup>-2</sup> and the capacity is 5 mAh cm<sup>-2</sup>. The COF layer was peeled off by tapes before observation.

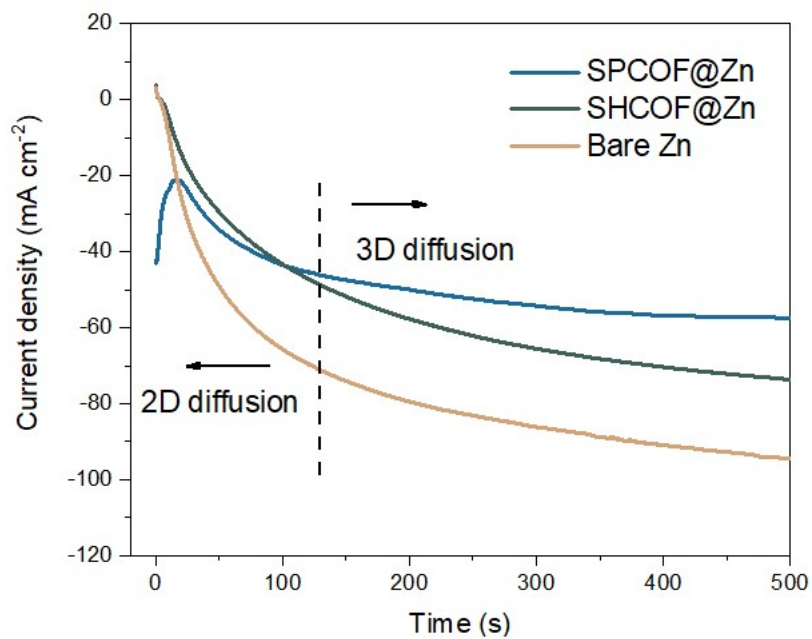


**Figure S36.** The CA curves of different Zn anodes tested in Zn||Zn symmetric cells using different electrolytes

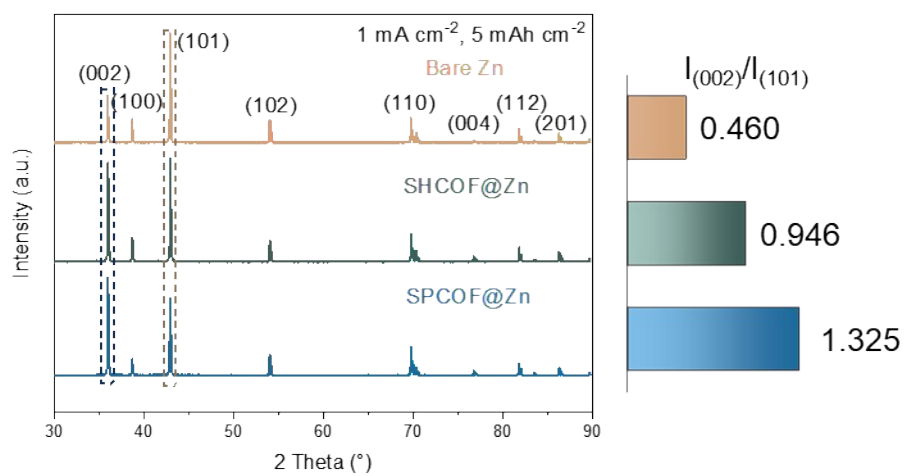


**Figure S37.** XRD patterns of deposited Zn on the different electrodes.

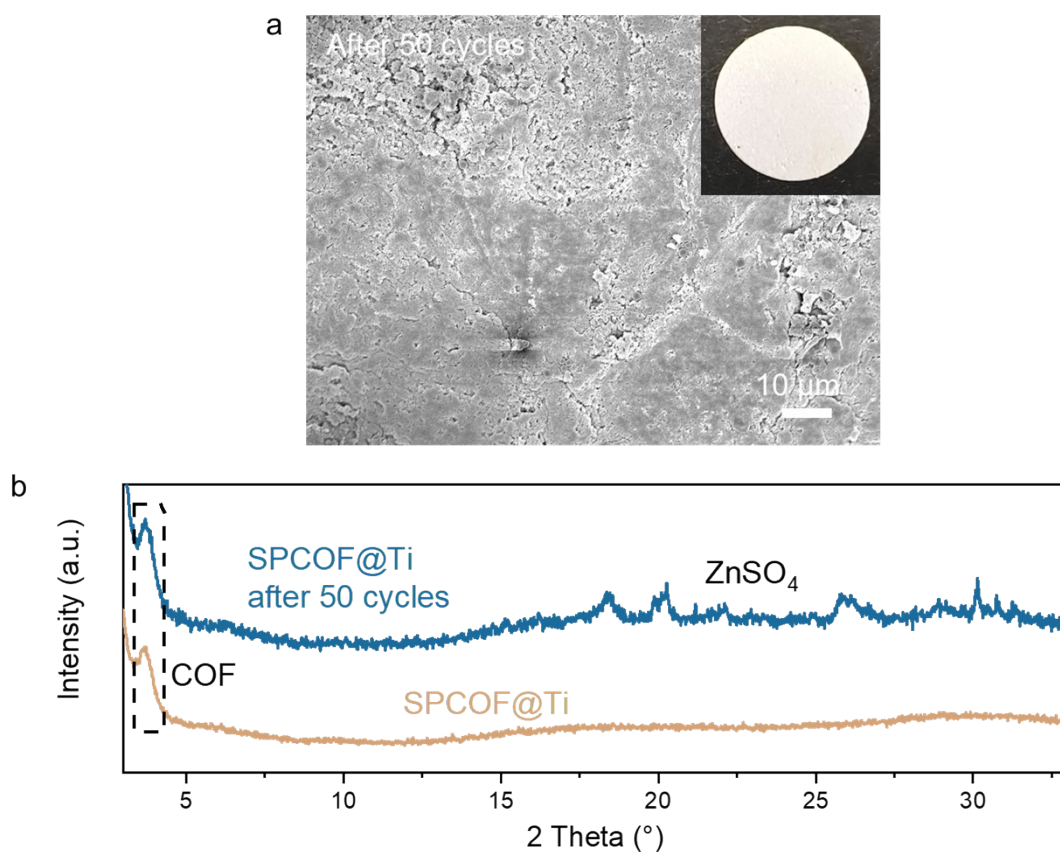


**Figure S38.** SEM images (a) and XRD patterns of SPCOF@Ti electrode (b) after 50 cycles stripping and plating ( $1 \text{ mA cm}^{-2}$ ,  $1 \text{ mAh cm}^{-2}$ ).

#### **Discussion for Zn deposition process:**

The optical morphological evaluation of the Zn deposition process was in-situ monitored via optical microscopy imaging within a transparent symmetrical battery device at a current density of  $10 \text{ mA cm}^{-2}$  and a capacity of  $10 \text{ mAh cm}^{-2}$  (Figure S33). Figure S29a illustrates the inhomogeneous deposition of Zn on a bare Zn substrate, which evolves into a mossy structure with an average thickness of approximately  $60 \text{ μm}$  after a 60-minute deposition period. The COF layer provides some suppression of dendritic Zn growth, although dendritic structures remain noticeable after 30 minutes (Figure S33b). In stark contrast, deposition on SPCOF@Zn is uniform, with no obvious dendrites observed throughout the plating process, showcasing effective suppression of dendrite growth and side reactions (Figure S33c). Post-deposition surface morphology observations of the zinc anodes reveal distinct differences. Cross-sectional SEM images and digital images of the SPCOF@Ti electrode after Zn deposition were obtained, as

shown in Figure S34. This can verify that Zn plating below the COF layer. The bare zinc anode shows numerous large flakes in random orientations after plating at  $1 \text{ mA cm}^{-2}/ 5 \text{ mAh cm}^{-2}$  (Figure S35a), attributed to insufficient ion migration dynamics and prevalent side reactions. In the SHCOF@Zn anode (Figure S35b), while the surface is mostly dense, dendritic Zn growth occurs within cracks, potentially leading to accumulative effects and eventual battery failure over multiple cycles. Conversely, the SPCOF@Zn anode (Figure S35c) displays ultra-dense and uniform zinc deposition with minimal crack formation under identical conditions. This uniform zinc deposition behavior with the SPCOF layer is further reflected in chronoamperometry curves (Figure S37). XRD patterns of the Zn deposits (Figure S37) indicate a stronger intensity of the (002) plane and a weaker intensity of the (100) plane for deposits protected by SPCOF compared to those on bare Zn. In zinc's crystalline structure, dendritic growth is primarily facilitated by the unsmooth and wavy arrangement of the (100) and (101) crystal planes, whereas the more smoothly surfaced (002) crystal planes promote a dendrite-free metal anode. These observations confirm that the growth of the Zn (002) plane is effectively promoted by the SPCOF layer. Additionally, to assess the impact of Zn deposition on the COF layer, XRD analysis and SEM imaging after 50 round Zn stripping/plating were performed (Figure S38). The results indicate that the COF layer retains a morphology and crystallinity similar to its uncycled state, further validating its structural stability.

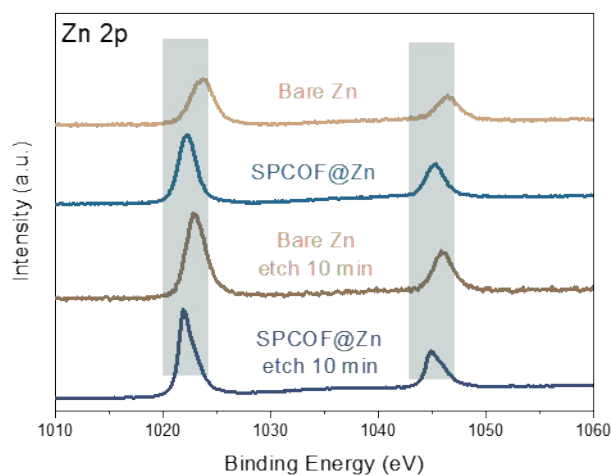


**Figure S39.** Zn 2p XPS peaks of deposited Zn on various electrodes before and after

cycles.

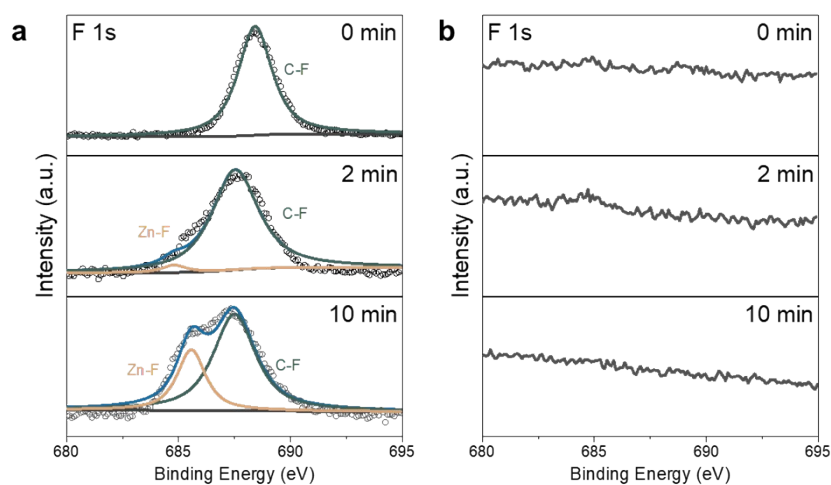


**Figure S40.** F 1s XPS peaks of deposited Zn on various electrodes along etching time.

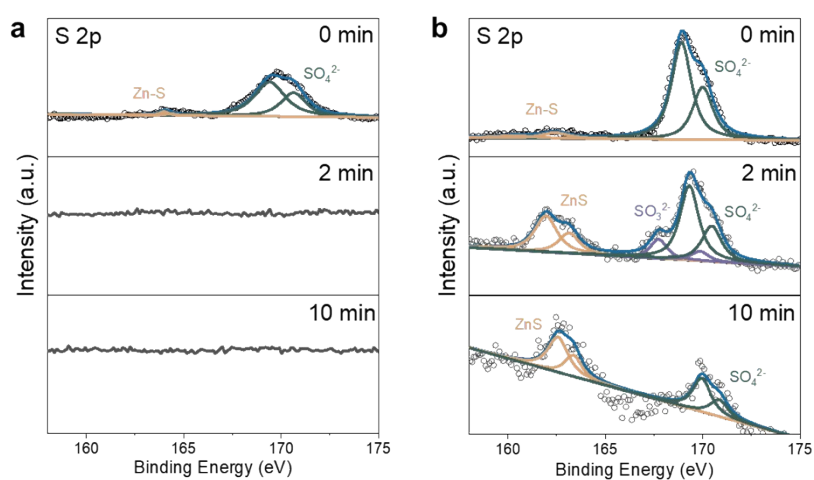


**Figure S41.** S 2p XPS peaks of deposited Zn on various electrodes along etching time.

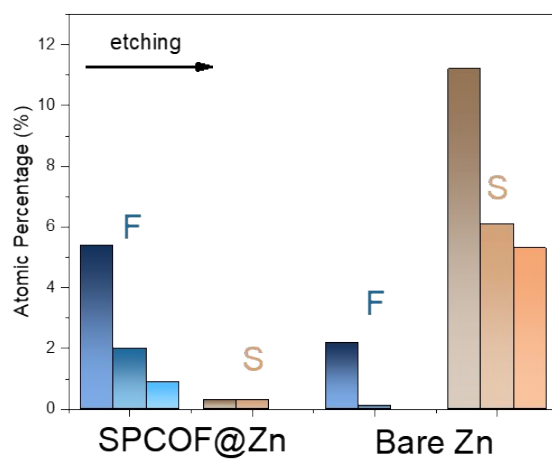


**Figure S42.** The comparison of atomic percentage of SPCOF@Zn and Zn anodes along

etching time.

### **Discussion for XPS patterns for Zn deposited layer:**

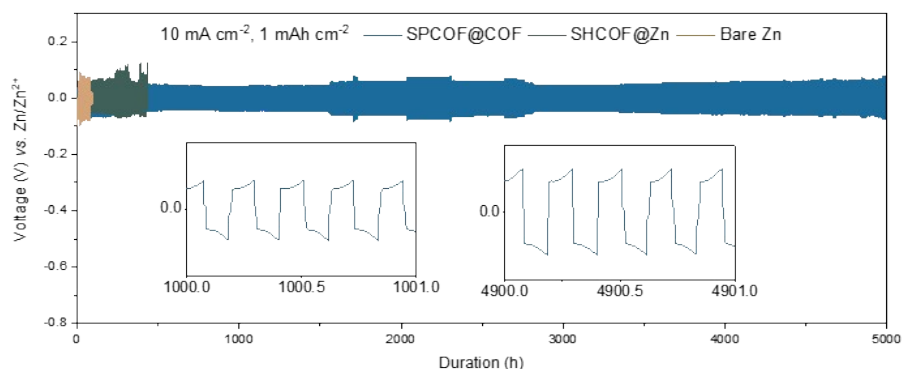
The comprehensive analysis of the bare Zn and SPCOF@Zn electrodes after cycling using X-ray Photoelectron Spectroscopy (XPS) with Argon ion ( $\text{Ar}^+$ ) etching provides significant insights into the chemical states present on the electrode surfaces. This analysis is critical for understanding the electrochemical behavior and stability of the electrodes in a  $\text{ZnSO}_4$  electrolyte. The findings are depicted in Figure S39-42.

Figure S39 presents the Zn2p spectrum, which showcases two characteristic peaks corresponding to Zn 2p<sub>1/2</sub> and Zn 2p<sub>3/2</sub>. The peaks located at 1021.4 eV and 1044.4 eV are indicative of the oxidized Zn ( $\text{Zn}^{2+}$ ) state, a signature of oxidation or corrosion products. Conversely, the peaks at 1020.2 eV and 1043.3 eV correspond to elemental Zn metal. The co-existence of peaks for  $\text{Zn}^{2+}$  and elemental Zn indicates the presence of both metallic Zn and byproducts, such as Zn salts formed during cycling. The high intensity of the  $\text{Zn}^{2+}$  and sulfur peaks in the spectrum particularly points to a significant accumulation of byproducts in cases where  $\text{ZnSO}_4$  electrolyte is employed.

After cycling, the Zn 2p spectrum of the SPCOF@Zn electrode exhibits a noticeable blue shift. This shift is attributed to the reduced formation of side products, highlighting effective stabilization and protection provided by the SPCOF layer against aggressive electrolyte environments. Additionally, lesser sulfur (S 2p) and more fluorine (F 1s) signatures are observed on the SPCOF@Zn surface post-cycling (Figure S40-42). This alteration in the chemical composition on the surface underscores the SPCOF layer's role in significantly suppressing the hydrogen evolution reaction and mitigating the formation of byproducts.

These observations, derived from the XPS analysis after cycling, demonstrate that the incorporation of the SPCOF layer on the Zn electrode enhances its resistance to degradation and undesirable reactions such as HER. The SPCOF layer acts as a barrier, reducing the interaction between the Zn metal and the aggressive components of the  $\text{ZnSO}_4$  electrolyte. This contributes to improved cyclic stability and maintains the integrity of the Zn electrode, making the SPCOF@Zn a more robust and durable option

in battery technologies.



**Figure S43.** Galvanostatic Zn stripping/plating behavior in Zn||Zn symmetric cells with different modification layers at 10 mA cm<sup>-2</sup> with a 1 mAh cm<sup>-2</sup> capacity.

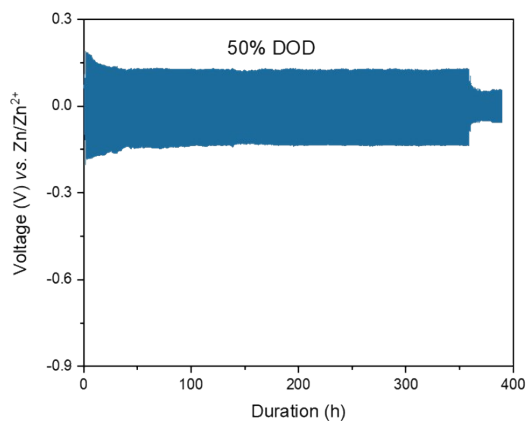


**Figure S44.** Galvanostatic Zn stripping/plating behavior in symmetric Zn cells with an SPCOF layer, demonstrated at an area capacity of 5.75 mAh cm<sup>-2</sup> (50% depth of discharge, DOD), and conducted at the same current density of 5.75 mA cm<sup>-2</sup> using ultrathin Zn foils (20 μm).

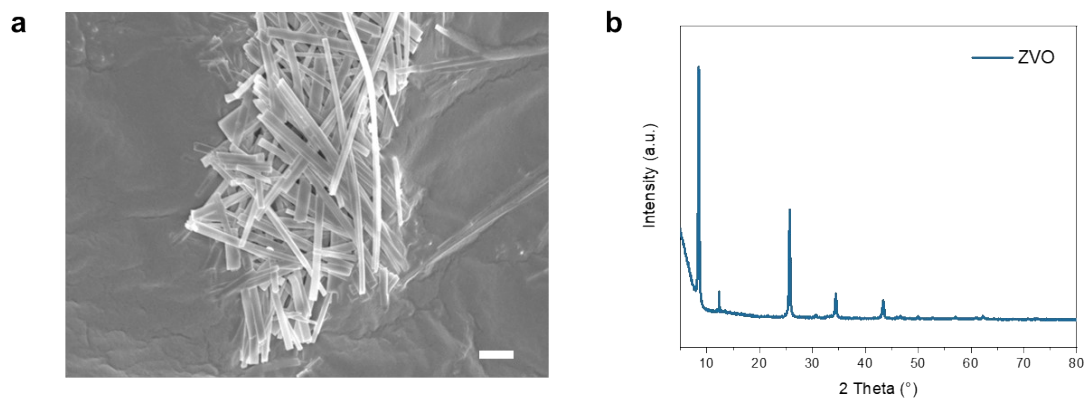


**Figure S45.** SEM image and XRD patterns of as prepared ZVO, scale bar: 1  $\mu\text{m}$ .

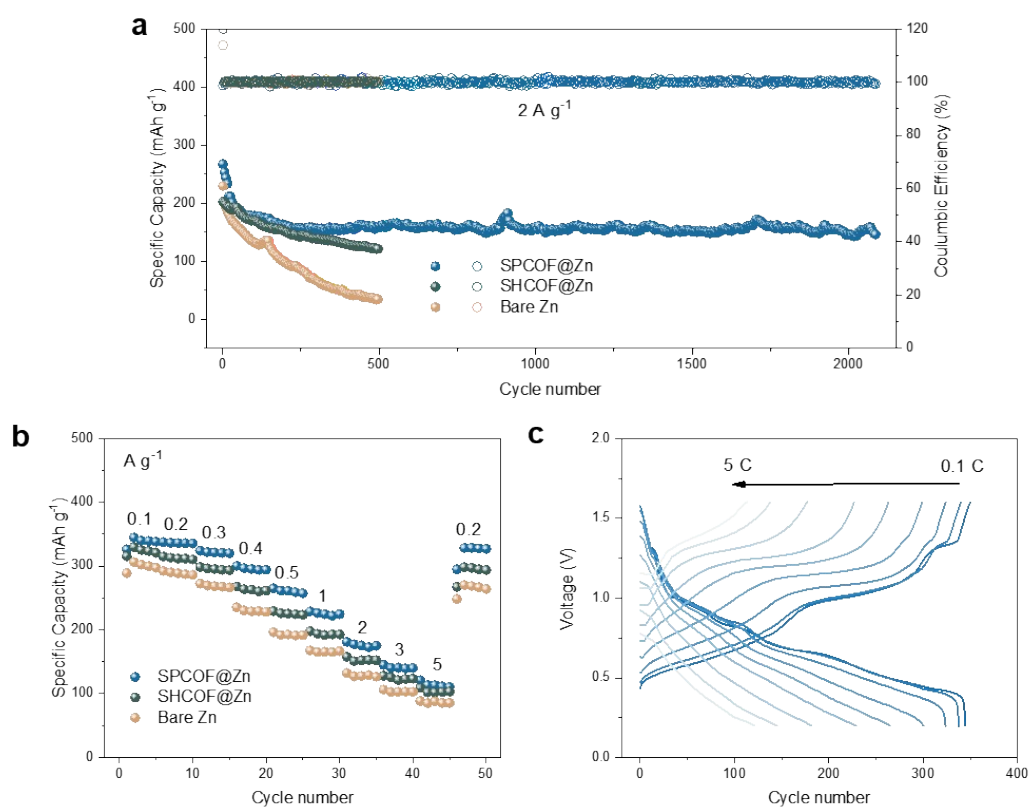


**Figure S46.** (a) Cycling performance of Zn||ZVO batteries featuring different electrodes in a 2M  $\text{ZnSO}_4$  electrolyte. (b) Rate capacity of Zn||ZVO batteries at different current densities and corresponding galvanostatic charge-discharge profiles.

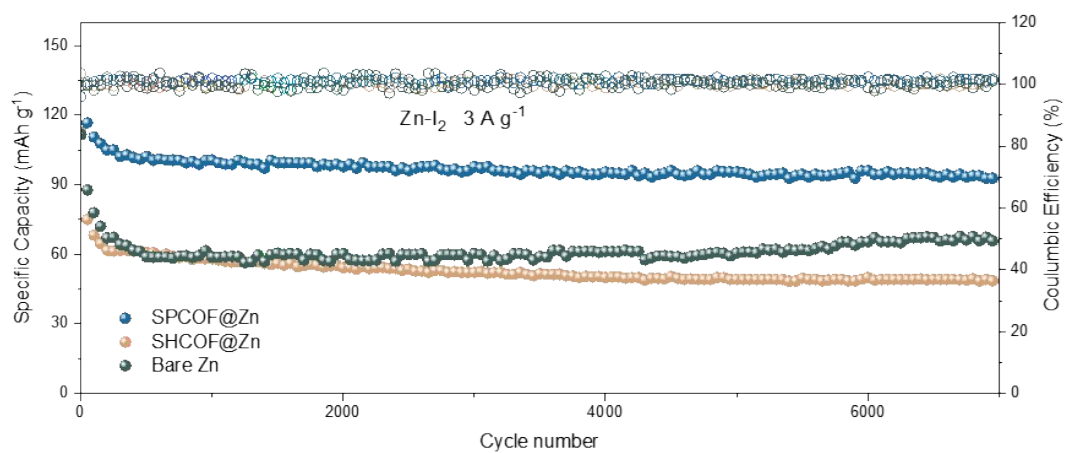


**Figure S47.** Cycling performance of Zn||I<sub>2</sub> batteries featuring different electrodes in a 2M ZnSO<sub>4</sub> electrolyte

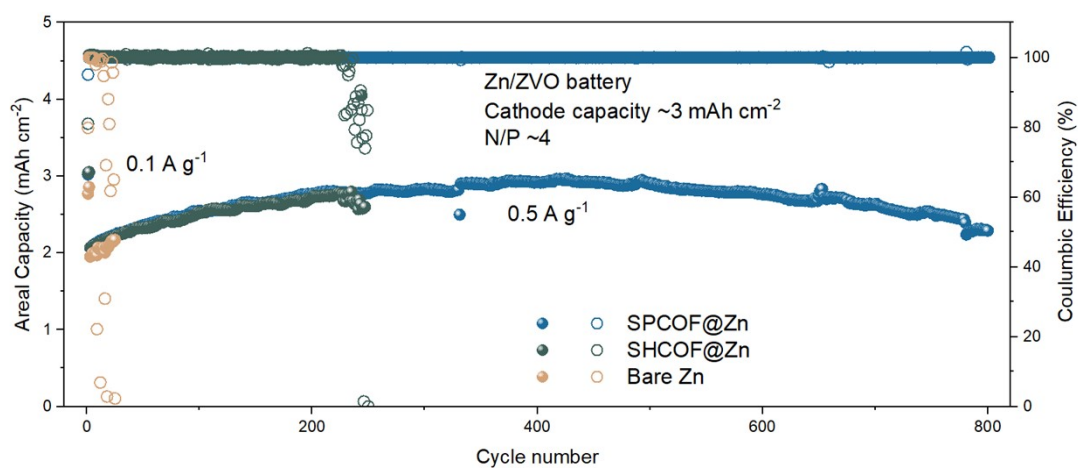


**Figure S48.** Cycling performance of Zn||ZVO batteries showcasing different electrodes in a 2M ZnSO<sub>4</sub> electrolyte at a low N/P ratio of ~4.

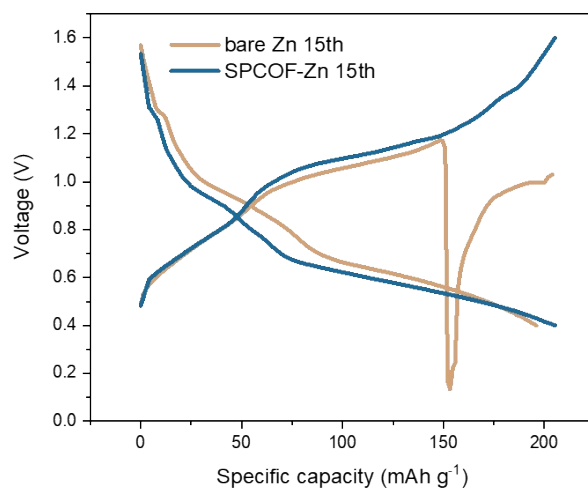


**Figure S49.** galvanostatic charge-discharge profiles of 15<sup>th</sup> cycles of Zn||ZVO with bare Zn anode and SPCOF@Zn anode at N/P ratio of 2.

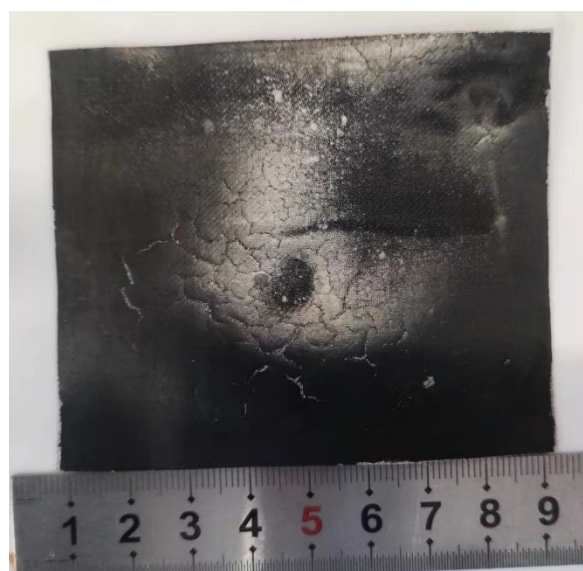


**Figure S50.** Optical images of as prepared high-loading ZVO cathodes, the loading of ZVO is  $\sim 20 \text{ mg cm}^{-2}$ .

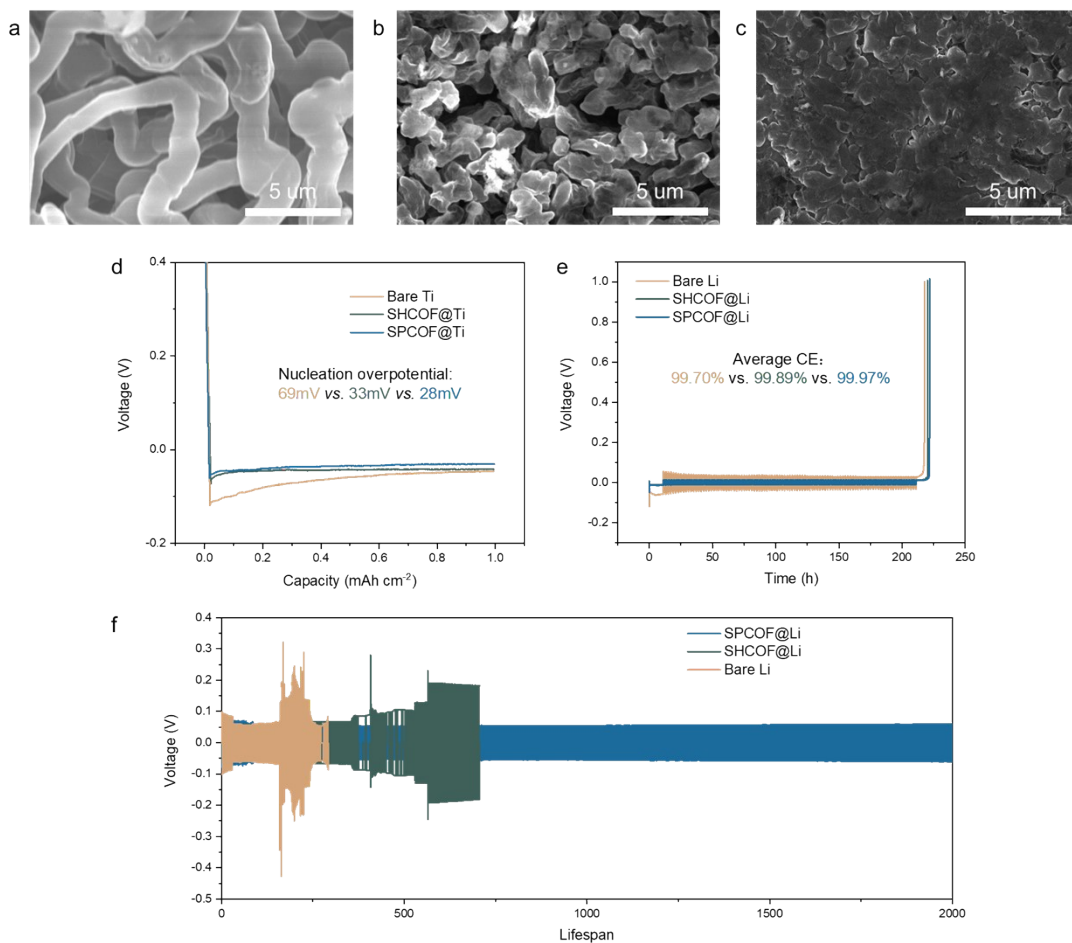


**Figure 51.** (a-c) Morphology of deposited Li with a capacity of  $1 \text{ mAh cm}^{-2}$  and a current density of  $1 \text{ mA cm}^{-2}$ , the modification layer has been peeled of layer by layer by tapes: (a) bare Li, (b) SHCOF@Li, (c) SPCOF@Li. (d) Nucleation overpotential on different electrodes. (e) Average coulombic efficiency determined by Aurbach test of different electrode. (f) cycling performance of the symmetrical Li cells with different electrodes at a current density of  $1 \text{ mA cm}^{-2}$ .

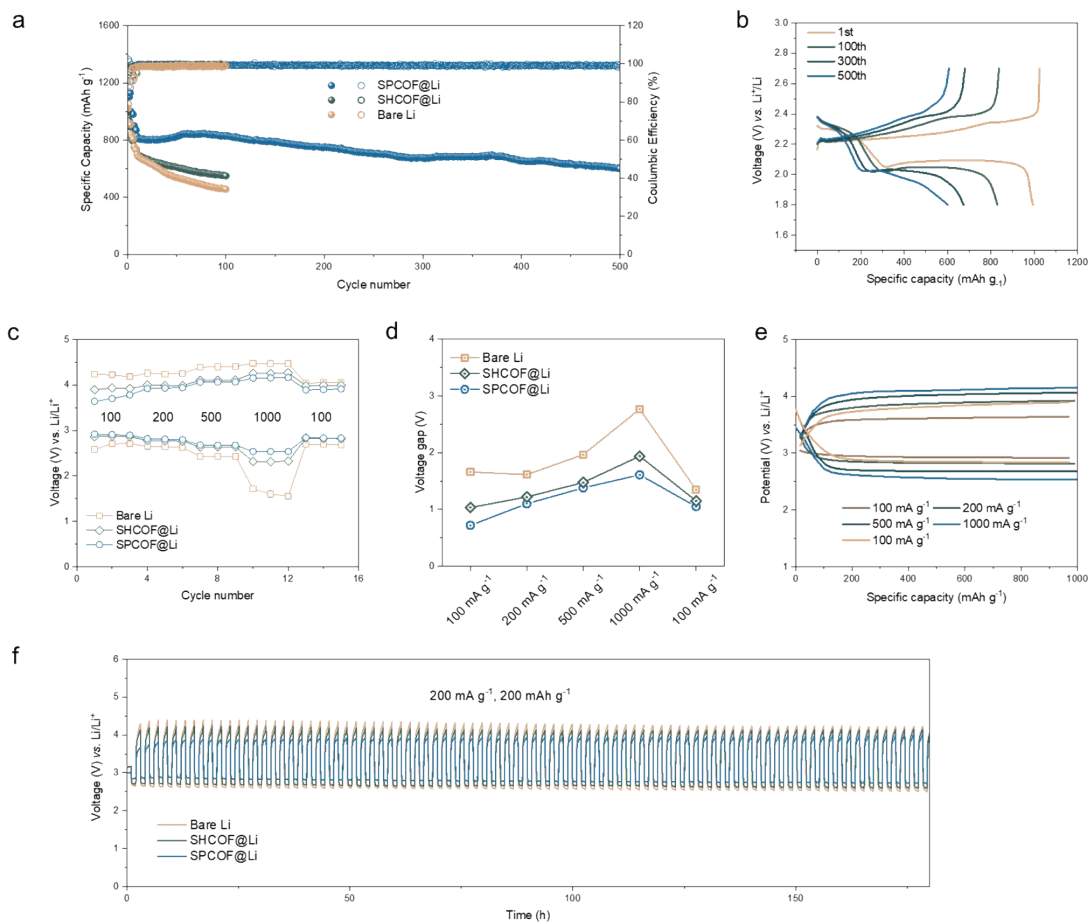


**Figure 52.** Application of SPCOF layer in different battery system: (a) Cycling stability of Li-S battery at a rate of 1C. (b) Corresponding charge-discharge curves of SPCOF@Li-S battery with different cycles. (c, d) Rate performances of Li-CO<sub>2</sub> batteries within a limiting capacity of 1000 mAh g<sup>-1</sup> at various current densities and corresponding voltage gap. (e) Corresponding charge-discharge curves of SPCOF@Li-CO<sub>2</sub> battery at different current densities. (f) Cycling stability of Li-CO<sub>2</sub> battery at 200 mA g<sup>-1</sup> and 200 mAh g<sup>-1</sup>.

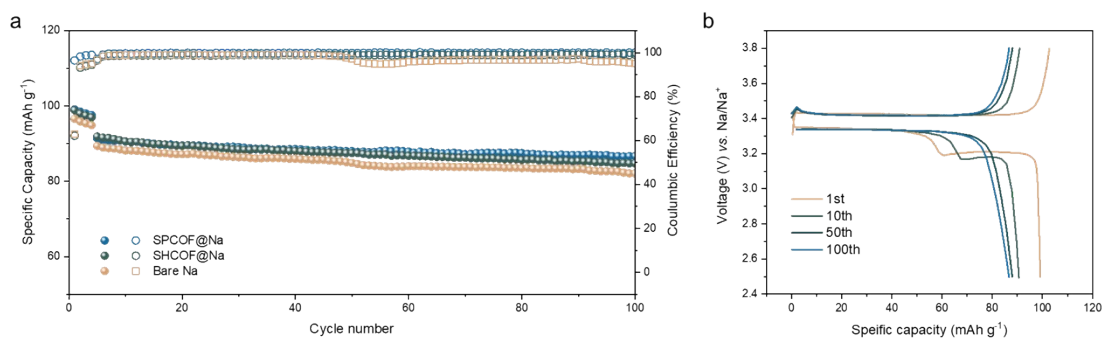


**Figure S53.** Cycling stability of Na-NVP at a rate of 2C by SPCOF@Na, SHCOF@Na and bare Na electrode and corresponding charge-discharge curves of SPCOF@Na-NVP batteries at different cycles.

**Table S1.** Summary of electrochemical performance of recently typical Zn anode with different strategies

Strategies	Current density (mA cm <sup>-2</sup> )	Time (h)	Cumulative capacity (Ah cm <sup>-2</sup> )	Ref.
MPVMT	50	300	7.5	6
	1	2000	1	
Sn@NHCF	1	370	0.185	7
HTFSI	2	2000	4	8
AA <sub>n</sub> -COF	20	300	3.75	9
SAB	10	300	3	10
PCu	10	200	1	11
PS-Zn	10	500	2.5	12
DESM				13
Zn <sub>5</sub> Cu	2.5	1600	2	14
FCOF	8	750	3	15
PVDF-Sn	5	500	1.25	16
	1	1200	0.6	
SPCOF	1	5000	2.5	Our work
	10	4900	24.5	

**Table S2.** Summary of electrochemical performance of recently typical Zn anode with different strategies

Strategies	N/P ratio	Cycle number	Cumulative capacity (mAh cm <sup>-2</sup> )	Ref.
C <sub>3</sub> N <sub>4</sub>	1.85	>400	2550	17
FCOF	2	250	250	15
ZAP	1.44	110	440	18
N,P-CMF	2.91	200	580	19
CFTA	2.58	500	1700	20
DEE	1.5	400	1800	21
MPVMT	1.9	200	600	6
Zn[0001]	37.4	450	900	22
C <sub>3</sub> N <sub>4</sub> QDs	524.4	3000	675	23
PVDF-Sn	13.1	250	900	16
SAB	3.65	500	1035	10
ZnBF <sub>4</sub> /ED	22.3	800	360	24
MeOH	9.4	800	504	25
ZnF <sub>2</sub> -SEI	2	1000	450	26
PSPMA	122.9	800	190	27
SPS10	32.5	200	360	28
<b>SPCOF</b>	<b>~2</b>	<b>&gt;500</b>	<b>2721</b>	<b>This work</b>
	<b>~4</b>	<b>&gt;800</b>	<b>4400</b>	

## Reference

- [1] S. J. J. o. c. p. Plimpton, *Journal of computational physics* 1995, **117**, 1.
- [2] A. Gabrieli, M. Sant, P. Demontis, G. B. Suffritti, *J. Chem. Theory. Comput.* 2015, **11**, 3829.
- [3] D. E. Coupry, M. A. Addicoat, T. Heine, *J. Chem. Theory. Comput.* 2016, **12**, 5215.
- [4] X. Wang, W. Wang, Y. Liu, M. Ren, H. Xiao and X. J. A. c. Liu, *Anal. Chem.*, 2016, **88**, 3926-3934.
- [5] Y. Li, J. Cheng, X. Wang, Y. Liu and X. J. P. C. C. P. Liu, *Phys. Chem. Chem. Phys.*, 2021, **23**, 26853-26863.
- [6] L. Han, Y. Guo, F. Ning, X. Liu, J. Yi, Q. Luo, B. Qu, J. Yue, Y. Lu, Q. Li, *Adv. Mater.* 2024, **36**, e2308086.
- [7] H. Yang, Y. Qiao, Z. Chang, H. Deng, X. Zhu, R. Zhu, Z. Xiong, P. He, H. Zhou, *Adv. Mater.* 2021, **33**, e2102415.
- [8] Z. Zheng, X. Zhong, Q. Zhang, M. Zhang, L. Dai, X. Xiao, J. Xu, M. Jiao, B. Wang, H. Li, Y. Jia, R. Mao, G. Zhou, *Nat. Commun.* 2024, **15**, 753.
- [9] H. Yu, Y. Zeng, N. W. Li, D. Luan, L. Yu, X. W. J. S. A. Lou, *Sci. Adv.* 2022, **8**, eabm5766.
- [10] Q. Nian, X. Luo, D. Ruan, Y. Li, B. Q. Xiong, Z. Cui, Z. Wang, Q. Dong, J. Fan, J. Jiang, J. Ma, Z. Ma, D. Wang, X. Ren, *Nat. Commun.* 2024, **15**, 4303.
- [11] C. Guo, J. Zhou, Y. Chen, H. Zhuang, Q. Li, J. Li, X. Tian, Y. Zhang, X. Yao, Y. Chen, S. L. Li, Y. Q. Lan, *Angew. Chem. Int. Ed.* 2022, **61**, e202210871.
- [12] S. Chen, Y. Xia, R. Zeng, Z. Luo, X. Wu, X. Hu, J. Lu, E. Gazit, H. Pan, Z. Hong, M. Yan, K. Tao, Y. Jiang, *Sci. Adv.* 2024, **10**, eadn2265.
- [13] J. Zhou, F. Wu, Y. Mei, Y. Hao, L. Li, M. Xie, R. Chen, *Adv. Mater.* 2022, **34**, e2200782.
- [14] Q. Li, A. Chen, D. Wang, Y. Zhao, X. Wang, X. Jin, B. Xiong, C. Zhi, *Nat. Commun.* 2022, **13**, 3699.
- [15] S. Zhai, W. Song, K. Jiang, X. Tan, W. Zhang, Y. Yang, W. Chen, N. Chen, H. Zeng, H. Li, Z. Li, *Energy & Environ. Sci.* 2023, **16**, 5479.

- [16] J. Ji, Z. Zhu, H. Du, X. Qi, J. Yao, H. Wan, H. Wang, L. Qie, Y. Huang, *Adv. Mater.* 2023, **35**, e2211961.
- [17] Z. Zhao, R. Wang, C. Peng, W. Chen, T. Wu, B. Hu, W. Weng, Y. Yao, J. Zeng, Z. Chen, P. Liu, Y. Liu, G. Li, J. Guo, H. Lu, Z. Guo, *Nat. Commun.* 2021, **12**, 6606.
- [18] Q. Cao, Y. Gao, J. Pu, X. Zhao, Y. Wang, J. Chen, C. Guan, *Nat. Commun.* 2023, **14**, 641.
- [19] W. Zhang, Q. Zhao, Y. Hou, Z. Shen, L. Fan, S. Zhou, Y. Lu, L. A. J. S. A. Archer, *Sci. Adv.* 2021, **7**, eabl3752.
- [20] N. Yang, Y. Gao, F. Bu, Q. Cao, J. Yang, J. Cui, Y. Wang, J. Chen, X. Liu, C. Guan, *Adv. Mater.* 2024, **36**, e2312934.
- [21] Y. Zeng, Z. Pei, D. Luan, X. W. D. Lou, *J. Am. Chem. Soc.* 2023, **145**, 12333.
- [20] Q. Liu, X. Liu, Y. Liu, M. Huang, W. Wang, Y. Cheng, H. Zhang, L. Xu, *ACS Nano* 2024, **18**, 4932.
- [22] C. Liu, W. Xu, L. Zhang, D. Zhang, W. Xu, X. Liao, W. Chen, Y. Cao, M. C. Li, C. Mei, K. Zhao, *Angew. Chem. Int. Ed.* 2024, **63**, e202318063.
- [23] X. Zhang, J. Li, Y. Liu, B. Lu, S. Liang, J. Zhou, *Nat. Commun.* 2024, **15**, 2735.
- [24] W. Zhang, M. Dong, K. Jiang, D. Yang, X. Tan, S. Zhai, R. Feng, N. Chen, G. King, H. Zhang, H. Zeng, H. Li, M. Antonietti, Z. Li, *Nat. Commun.* 2022, **13**, 5348.
- [25] D. Han, C. Cui, K. Zhang, Z. Wang, J. Gao, Y. Guo, Z. Zhang, S. Wu, L. Yin, Z. Weng, F. Kang, Q.-H. Yang, *Nat. Sustain.* 2021, **5**, 205.
- [26] L. Ma, J. Vatamanu, N. T. Hahn, T. P. Pollard, O. Borodin, V. Petkov, M. A. Schroeder, Y. Ren, M. S. Ding, C. Luo, J. L. Allen, C. Wang, K. Xu, *Proc. Natl. Acad. Sci. U. S. A.* 2022, **119**, e2121138119.
- [27] L. Cao, D. Li, T. Pollard, T. Deng, B. Zhang, C. Yang, L. Chen, J. Vatamanu, E. Hu, M. J. Hourwitz, L. Ma, M. Ding, Q. Li, S. Hou, K. Gaskell, J. T. Fourkas, X. Q. Yang, K. Xu, O. Borodin, C. Wang, *Nat. Nanotechnol.* 2021, **16**, 902.
- [28] H. Liu, Q. Ye, D. Lei, Z. Hou, W. Hua, Y. Huyan, N. Li, C. Wei, F. Kang, J.-G. Wang, *Energy & Environ. Sci.* 2023, **16**, 1610.